

Mid- to far-infrared properties of star-forming galaxies and active galactic nuclei

G. E. Magdis, D. Rigopoulou, G. Helou, D. Farrah, P. Hurley, A. Alonso-Herrero, J. Bock, D. Burgarella, S. Chapman, V. Charmandaris, et al.

▶ **To cite this version:**

G. E. Magdis, D. Rigopoulou, G. Helou, D. Farrah, P. Hurley, et al.. Mid- to far-infrared properties of star-forming galaxies and active galactic nuclei. Astronomy and Astrophysics - A&A, 2013, 558, pp.A136. 10.1051/0004-6361/201322226 . cea-01135443

HAL Id: cea-01135443
https://cea.hal.science/cea-01135443

Submitted on 25 Mar 2015

HAL is a multi-disciplinary open access archive for the deposit and dissemination of scientific research documents, whether they are published or not. The documents may come from teaching and research institutions in France or abroad, or from public or private research centers.

L'archive ouverte pluridisciplinaire **HAL**, est destinée au dépôt et à la diffusion de documents scientifiques de niveau recherche, publiés ou non, émanant des établissements d'enseignement et de recherche français ou étrangers, des laboratoires publics ou privés.

A&A 558, A136 (2013)
DOI: 10.1051/0004-6361/201322226
© ESO 2013

Astronomy & Astrophysics

Mid- to far-infrared properties of star-forming galaxies and active galactic nuclei⋆,⋆⋆

G. E. Magdis[1], D. Rigopoulou[1,2], G. Helou[3], D. Farrah[4], P. Hurley[5], A. Alonso-Herrero[6,7], J. Bock[8,9], D. Burgarella[10], S. Chapman[11], V. Charmandaris[12,13,14], A. Cooray[15], Y. Sophia Dai[16], D. Dale[17], D. Elbaz[18], A. Feltre[19,20], E. Hatziminaoglou[20], J.-S. Huang[16,21], G. Morrison[22,23], S. Oliver[5], M. Page[24], D. Scott[25], and Y. Shi[26]

[1] Department of Physics, University of Oxford, Keble Road, Oxford OX1 3RH, UK
e-mail: georgios.magdis@astro.ox.ac.uk
[2] Space Science & Technology Department, Rutherford Appleton Laboratory, Chilton, Didcot, Oxfordshire OX11 0QX, UK
[3] Infrared Processing and Analysis Center, California Institute of Technology, Pasadena, CA 91125, USA
[4] Virginia Polytechnic Institute and State University Department of Physics, MC 0435, 910 Drillfield Drive, Blacksburg, VA 24061, USA
[5] Astronomy Centre, Department of Physics and Astronomy, University of Sussex, Falmer, Brighton BN1 9QH, UK
[6] Instituto de Fisica de Cantabria, CSIC-UC, 39005 Santander, Spain
[7] Augusto G. Linares Senior Research Fellow
[8] California Institute of Technology, 1200 E. California Boulevard, Pasadena, CA 91125, USA
[9] Jet Propulsion Laboratory, 4800 Oak Grove Drive, Pasadena, CA 91109, USA
[10] Aix-Marseille Université, CNRS, LAM (Laboratoire d'Astrophysique de Marseille), 13388 Cedex 13 Marseille, France
[11] Dalhousie University, Halifax, Nova Scotia B3H 4R2, Canada
[12] Department of Physics and ITCP, University of Crete, 71003 Heraklion, Greece
[13] IESL/Foundation for Research and Technology – Hellas, 71110 Heraklion, Greece
[14] Observatoire de Paris, 75014 Paris, France
[15] Department of Physics & Astronomy, University of California, Irvine, CA 92697, USA
[16] Harvard-Smithsonian Center for Astrophysics, 60 Garden Street, MS65, Cambridge, MA 02138, USA
[17] Department of Physics and Astronomy, University of Wyoming, Laramie, WY 82071, USA
[18] Laboratoire AIM-Paris-Saclay, CEA/DSM/Irfu, CNRS, Université Paris Diderot, Saclay, 19190 Gif-sur-Yvette, France
[19] ESO, Karl-Schwarzschild-Str. 2 85748 Garching bei Munchen, Germany
[20] Dipartimento di Fisica e Astronomia, Vicolo Osservatorio 2, 35122 Padova, Italy
[21] National Astronomical Observatories, Chinese Academy of Sciences, 100012 Beijing, PR China
[22] Institute for Astronomy, University of Hawaii, Honolulu, HI 968226, USA
[23] Canada-France-Hawaii Telescope, Kamuela, HI 96743, USA
[24] Mullard Space Science Laboratory, University College London, Holmbury St Mary Dorking, Surrey RH5 6NT, WCIE6BT London, UK
[25] Department of Physics & Astronomy, University of British Columbia, 6224 Agricultural Road, Vancouver, BC V6T 1Z1, Canada
[26] School of Astronomy And Space Science, Nanjing University, Jiangsu 210093, PR China

Received 8 July 2013 / Accepted 23 August 2013

ABSTRACT

We study the mid- to far-IR properties of a 24 μm-selected flux-limited sample ($S_{24} > 5$ mJy) of 154 intermediate redshift ($\langle z \rangle \sim 0.15$), infrared luminous galaxies, drawn from the 5 Milli-Jansky Unbiased *Spitzer* Extragalactic Survey. By combining existing mid-IR spectroscopy and new *Herschel* SPIRE submm photometry from the *Herschel* Multi-tiered Extragalactic Survey, we derived robust total infrared luminosity ($L_{\rm IR}$) and dust mass ($M_{\rm dust}$) estimates and infered the relative contribution of the AGN to the infrared energy budget of the sources. We found that the total (8−1000 μm) infrared emission of galaxies with weak 6.2 μm PAH emission ($EW_{6.2} \leq 0.2$ μm) is dominated by AGN activity, while for galaxies with $EW_{6.2} > 0.2$ μm more than 50% of the $L_{\rm IR}$ arises from star formation. We also found that for galaxies detected in the 250–500 μm *Herschel* bands an AGN has a statistically insignificant effect on the temperature of the cold dust and the far-IR colours of the host galaxy, which are primarily shaped by star formation activity. For star-forming galaxies we reveal an anti-correlation between the $L_{\rm IR}$-to-rest-frame 8 μm luminosity ratio, IR8 $\equiv L_{\rm IR}/L_8$ and the strength of PAH features. We found that this anti-correlation is primarily driven by variations in the PAHs emission, and not by variations in the 5−15 μm mid-IR continuum emission. Using the [Ne III]/[Ne II] line ratio as a tracer of the hardness of the radiation field, we confirm that galaxies with harder radiation fields tend to exhibit weaker PAH features, and found that they have higher IR8 values and higher dust-mass-weighted luminosities ($L_{\rm IR}/M_{\rm dust}$), the latter being a proxy for the dust temperature ($T_{\rm d}$). We argue that these trends originate either from variations in the environment of the star-forming regions or are caused by variations in the age of the starburst. Finally, we provide scaling relations that will allow estimating $L_{\rm IR}$, based on single-band observations with the mid-infrared instrument, on board the upcoming *James Webb* Space Telescope.

Key words. galaxies: evolution – galaxies: active – galaxies: starburst – galaxies: star formation – infrared: galaxies

⋆ *Herschel* is an ESA space observatory with science instruments provided by European-led Principal Investigator consortia and with important participation from NASA.
⋆⋆ Tables 1 and 2 are available in electronic form at http://www.aanda.org

1. Introduction

One of the major advances in our understanding of galaxy evolution was the discovery of the cosmic infrared background (CIB), first detected by Puget et al. (1996), which led to the realisation that half of the energy produced by star formation and accretion activity throughout the history of the Universe is emitted via the infrared (8−1000 μm) part of the spectrum (Dole et al. 2006). Because in the local Universe the infrared output of galaxies is only about a third of the emission at optical wavelengths (e.g., Soifer & Neugebauer 1991), this implies a strong evolution of infrared galaxy populations, with an enhanced far-IR output in the past, to account for the total measured CIB.

With the advent of infrared space telescopes, such as the Infrared Space Observatory (Kessler et al. 1996; see Genzel & Cesarsky 2000, for a summary), the *Spitzer* Space Telescope (*Spitzer*, Werner et al. 2004), and more recently the *Herschel* Space Observatory (*Herschel*, Pilbratt et al. 2010) we have been able to resolve a considerable fraction of the CIB (e.g. ∼74% at 160 μm, Berta et al. 2011) into individual sources and construct and characterise large samples of infrared galaxies (for a review see Lagache et al. 2005). These infrared campaigns have revealed that the number density of luminous infrared galaxies (LIRGs $L_{\rm IR} > 10^{11}$ $L_{\odot}$) and ultra luminous infrared galaxies (ULIRGs $L_{\rm IR} > 10^{12}$ $L_{\odot}$), which emit the bulk of their energy in the infrared, increases by three orders of magnitude as we look back in time and they also dominate the star formation density of the Universe by $z \sim 1$ (e.g. Le Floc'h et al. 2005).

Different parts of the IR spectrum of galaxies are dominated by different physical processes. The mid-IR (5−25 μm) emission is dominated by warm dust emission, which originates from the small dust grains that are heated by energetic photons produced by young stars or through AGN accretion activity. Superimposed on this continuum emission is a large set of broad emission line features, centred at 3.3, 6.2, 7.7, 8.6, 11.2, and 12.7 μm, which are thought to originate from polycyclic aromatic hydrocarbons (PAHs; Puget et al. 1985; Allamandola et al. 1989). PAH emission predominantly originates from photodissociation regions (PDRs) that are illuminated by UV-bright stars and can contribute up to 10% of the total infrared luminosity ($L_{\rm IR}$) in star-forming galaxies (e.g. Smith et al. 2007). Previous *Spitzer* studies using the Infrared Spectrograph (IRS, Houck et al. 2004) have shown that PAH emission varies considerably between star-forming and AGN-dominated galaxies and as a function of the metal enrichment of the interstellar medium (ISM) of a galaxy. In particular, PAHs are found to be prominent in star-forming galaxies or weak AGNs both locally (Peeters et al. 2002, 2004; Weedman et al. 2005; Armus et al. 2007) and at high-z (Pope et al. 2008; Huang et al. 2009; Desai et al. 2009), while they tend to be weaker or even absent in galaxies dominated by an AGN (e.g. Kirkpatrick et al. 2012; Weedman et al. 2006). Hence, the strength and the relative ratio of the PAHs, along with a plethora of other atomic fine structure lines (e.g., Ne, S) and absorption by amorphous silicates centred at 9.7 μm, offer a unique diagnostic tool characterising the dominant mechanism that powers the IR emission of the galaxies (e.g., Laurent et al. 2000; Lutz et al. 1996; Genzel et al. 1998; Peeters et al. 2004; Spoon et al. 2007).

Mid-IR spectroscopic studies of local (Rigopoulou et al. 1999; Farrah et al. 2007; Desai et al. 2007) and distant (e.g., Yan et al. 2007; Dasyra et al. 2009; Hernan-Caballero et al. 2009) LIRGs and ULIRGs have revealed that while both AGN and star formation activity is present, their IR emission is mostly powered by star-formation. However, to properly measure the bolometric output of the galaxies there is an imperative need for far-IR (50–350 μm) observations that trace the peak of the spectral energy distribution (SED) of star-forming galaxies. Furthermore, while recent studies of high-z galaxies have come to suggest that the far-IR emission is primarily shaped by star formation activity (Hatziminaoglou et al. 2010; Kirkpatrick et al. 2012; Feltre et al. 2013), it is still unclear whether and how an AGN could impact the far-IR colours and the dust temperature of the large grains in the ISM of a galaxy (e.g. Haas et al. 2003; Netzer et al. 2007).

With the advent of *Herschel* we have now gained access to the far-IR part of the spectrum of the galaxies up to $z \sim 2$, and it is now possible to bridge the warm and cold dust emission and reveal the underlying heating mechanisms. In this direction, it has recently been demonstrated that for the majority of star-forming galaxies up to $z \sim 2$, the ratio of total ($L_{\rm IR}$) to the mid-IR luminosity, as traced by the rest-frame 8 μm emission (L_8), obeys an almost linear relation, suggesting a very uniform mid-to-far-IR SED shape for star-forming galaxies through cosmic time (Elbaz et al. 2011). However, outliers to this relation do exist, with a small fraction of star-forming galaxies exhibiting an enhanced IR8 $\equiv L_{\rm IR}/L_8$ value. While this excess in IR8 is found to anti-correlate with the IR surface brightness and hence with the projected star formation density (Elbaz et al. 2011), the true nature of these sources, the origin and the scatter of the observed $L_{\rm IR}-L_8$ relation among galaxies that fall in this "IR main sequence", and the connection of the mid- to the far-IR properties of the galaxies are yet to be fully understood.

Another key question that still remains open is whether the characteristics of the PAH features can be used to infer information about the star formation properties of the galaxies. In principle, PAHs could serve as a good tracer of star formation activity, since they are stochastically heated mainly by UV photons produced by stars (PAHs can also be excited by visual photons, although the excitation is dominated by UV photons; e.g., Uchida et al. 1998; Li & Draine 2002). Under the assumption of fixed emission and absorption properties and fixed PAH abundance, the PAH emission is a measure of the amount of photons available between 6 and 13.6 eV and hence of star formation. This line of reasoning is supported by various studies that have demonstrated an almost linear correlation between PAH emission and $L_{\rm IR}$ (e.g. Soifer et al. 2002; Peeters et al. 2004; Lutz et al. 2008), the latter thought to be an excellent tracer of star-formation rate for dusty circumnuclear starbursts (Kennicutt 1998). However, the $L_{\rm PAH}/L_{\rm IR}$ ratio is known to vary as a function of the environment in which star formation takes place (e.g., Peeters et al. 2004) but also as a function of AGN activity (e.g. Siebenmorgen et al. 2004). This also applies to integrated $L_{\rm PAH}$ and $L_{\rm IR}$ measurements over the whole galaxy. In particular, the $L_{\rm PAH}/L_{\rm IR}$ ratio can vary up to a factor 10 between sources where the environment of massive star formation resembles PDRs (e.g. M 82, Carral et al. 1994) and that of embedded star formation (e.g. Arp220) that is more similar to the properties of compact H II regions (Rigopoulou et al. 1999). Interestingly, a similar variation in the strength of far-IR fine structure lines is observed among different star formation environments (e.g. Gracia-Carpio et al. 2011). It could therefore be suggested that the integrated PAH properties of distant galaxies, where the individual star-forming regions remain unresolved, can carry crucial information about the averaged star formation activity on a galaxy-wide scale.

To address these questions, in this paper we exploit a 24 μm-flux-limited sample of intermediate redshift mid-IR-selected galaxies that benefit from high-quality mid-IR IRS spectra

obtained as part of the 5 Milli-Jansky Unbiased *Spitzer* Extragalactic Survey (5MUSES). By combining existing mid- and far-IR data with new submm (250−500 μm) *Herschel*-SPIRE observations drawn from the HerMES project, we attempt a full characterisation of their IR properties and study the variation of the PAH features among star-forming galaxies. A key aspect of our sample is that it traces the epoch of the steep increase of the infrared luminosity density ($0.0 \leq z \leq 1.0$), providing a snapshot of the evolution of the properties of star-forming galaxies from the present day to the peak of the star formation activity in the Universe ($z \sim 1-2$). In Sect. 2 we provide a description of the sample, present ancillary IRS and newly obtained *Herschel* data and classify the dominant powering source of the galaxies. In Sect. 3 we derive the far-IR properties of the sample, while in Sect. 4 we investigate the impact of the AGN activity on the far-IR properties of the galaxies and examine the variation of the strength of PAH features as a function of IR8. In Sect. 6 we provide a discussion motivated by our results, and finally in Sect. 7 we summarise our findings. Throughout the paper we adopt $\Omega_{\rm m} = 0.3$, $H_0 = 71$ km s^{-1} Mpc^{-1} and $\Omega_\Lambda = 0.7$.

2. Sample selection and observations

5MUSES is a 24 μm flux-limited (5 mJy $< S_{24} <$ 100 mJy), mid-IR spectroscopic survey of 330 galaxies selected from the SWIRE fields (Lonsdale et al. 2003), including Elais-N1, Elais-N2, Lockman Hole, and XMM-LSS, in addition to the *Spitzer* Extragalactic First Look Survey (XFLS) field (Fadda et al. 2006). Out of this sample we focus on the 280 sources presented by Wu et al. (2010), for which we have secure spectroscopic redshifts. This simple selection criterion of the 5MUSES survey provides an intermediate-redshift sample ($\langle z \rangle = 0.144$) they bridges the gap between the bright, nearby star-forming galaxies (e.g. Kennicutt et al. 2003; Smith et al. 2007; Dale et al. 2009; Pereira-Santaella et al. 2010; Diaz-Santos et al. 2010), local (U)LIRGs (e.g. Armus et al. 2007; Desai et al. 2007; Imanishi et al. 2007; Farrah et al. 2007; Veilleux et al. 2009), and the more distant sources that have been followed up with IRS spectroscopy (Houck et al. 2005; Sajina et al. 2007; Yan et al. 2007; Farrah et al. 2008; Pope et al. 2008; Desai et al. 2009; Menéndez-Delmestre et al. 2009; Sargsyan et al. 2011). Low-resolution mid-IR spectra ($R = 64-128$) of all galaxies in 5MUSES have been obtained with the short-low (SL: 5.5−14.5 μm) and long-low (LL: 14−35 μm) modules of the IRS using the staring mode observations. A full description of the IRS observations and data reduction are presented in Wu et al. (2010). In brief, PAH luminosities and equivalent width (EW) were measured using the PAHFIT software (Smith et al. 2007) as well as a spline-fitting method. In the former, the PAH features are fit with Drude profiles, which have extended wings that account for a significant fraction of the underlying plateau (Smith et al. 2007), while in the spline or apparent PAH EW method, a local continuum under the emission features is defined by fitting a spline function to selected continuum points. While the PAHFIT method is known to give higher integrated PAH fluxes and EWs due to the lower continuum adopted than the spline method, the two methods provide consistent results on trends (Smith et al. 2007; Galliano et al. 2008). Following Wu et al. (2010), we adopt PAH EWs as measured by the spline-fitting method, fixing the rest wavelength continuum pivots as in Peeters et al. (2002), and 6.2-, 7.7-, and 11.3 μm PAH-integrated fluxes as derived from PAHFIT. This was done to be able to compare our measurements with other samples reported in the literature, because the majority of these use the spline method when reporting EW values. Finally, in addition to the 24 μm photometry and IRS spectroscopy, the whole sample benefits from 70–160 μm MIPS and IRAC 3.6−8.0 μm observations, with 90% and 54% of the sources being detected at 70 and 160 μm, respectively.

2.1. Herschel observations

We used *Herschel* SPIRE (Griffin et al. 2010) observations of the fields ELAIS-N1, Lockman Hole, XMM, and XFLS, obtained as part of the *Herschel* Multi-Tiered Extragalactic Survey[1] (HerMES; Oliver et al. 2010, 2012). For these sources, we employed the photometric catalogues at 250, 350, and 500 μm that were produced for each field by using a prior source extraction, guided by the position of known 24 μm sources. An extensive description of the cross-identification prior source extraction (XID) method is given in Roseboom et al. (2010, 2012). The main advantage of this method is that reliable fluxes can be extracted close to the formal ≈4−5 mJy SPIRE confusion noise (Nguyen et al. 2010) by estimating the flux contributions from nearby sources within one beam. The 24 μm prior positional information reduces the impact of confusion noise and so the approximate 3σ limit for the SPIRE catalogue at 250 μm is ≈9−15 mJy. The drawback of this technique is that the resulting catalogues could be missing sources without a 24 μm counterpart, that is, 24 μm drop-outs (e.g. Magdis et al. 2011). However, since all galaxies in the 5MUSES sample have a bright 24 μm counterpart, we are not affected by this caveat.

Out of the 280 sources in the 5MUSES sample presented by Wu et al. (2010), 188 galaxies are covered by HerMES observations. After applying a flux cut limit of 15 mJy to all three bands of our SPIRE photometric catalogues, 154 sources are detected at 250 μm at a 3σ significance level, 108 at 350 μm, and 50 at 500 μm. All sources detected at 350 and 500 μm are also detected at 250 μm. To assess the robustness of the detections we also preformed a visual inspection of the sources in the *Herschel* maps. The SPIRE photometry of the final sample, that is, sources with at least one detection at one of the *Herschel* bands, is presented in Table 1. The spectroscopic redshifts of the sources are drawn from Wu et al. (2010) and the median redshift of the sample considered here is $\langle z \rangle = 0.157$. Finally, a K−S test reveals that the S_{250} values of the whole population of galaxies in our fields with $S_{24} > 5$ mJy and that of the 5MUSES sample are drawn from the same distribution. While this was expected based on the simple selection criteria of the 5MUSES samples ($S_{24} > 5$ mJy), it also suggests that it is representative of the full HerMES population at this 24 μm flux limit.

2.2. Classification of AGN and star-formation-dominated sources

The equivalent widths of PAH features can serve as indicators of the AGN versus star formation activity in the galaxy (e.g. Laurent et al. 2000; Brandl et al. 2006; Spoon et al. 2007). Here, we used the 6.2 μm equivalent width as measured by the spline-fit method. We chose the 6.2 over the 11.3 μm PAH band because the latter is located on the shoulder of the 9.7 μm silicate feature. Following previous studies (e.g., Armus et al. 2007; Wu et al. 2010), we classified sources with $EW_{6.2} \leq 0.2$ μm as AGN-dominated and sources with $EW_{6.2} > 0.2$ μm as composite

[1] For more information about the HerMES programme visit `hermes.sussex.ac.uk`

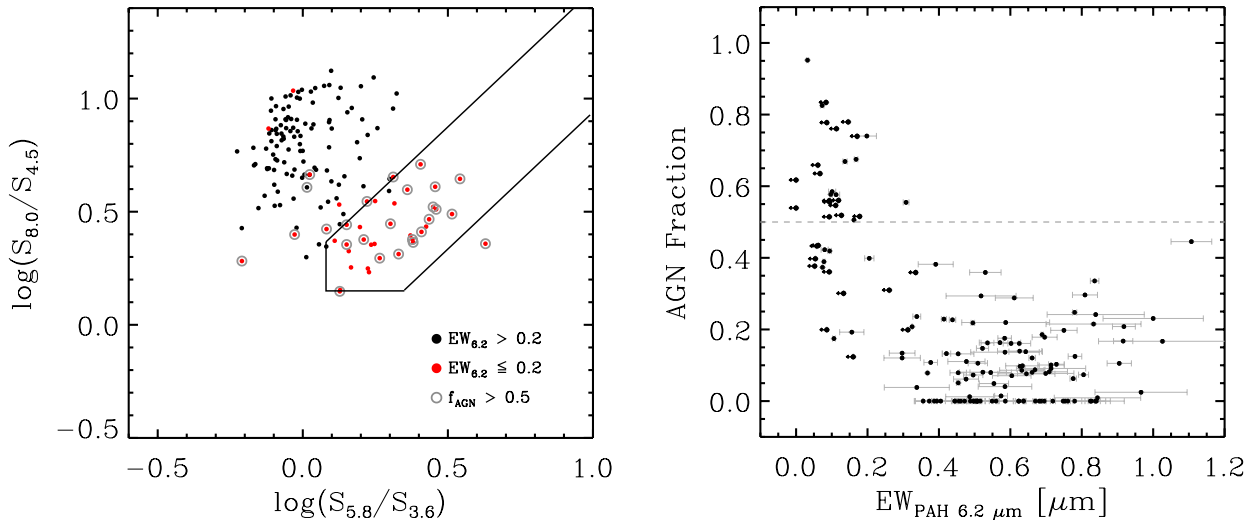


Fig. 1. *Left*: IRAC colour-colour diagram of the 5MUSES sample. The wedge is the AGN selection region of Donley et al. (2012). Red and black circles represent sources with $EW_{6.2} \leq 0.2$ μm and $EW_{6.2} > 0.2$ μm respectively. Grey circles correspond to sources for which the SED decomposition attributes more than 50% of their total infrared luminosity to AGN activity. *Right*: fractional contribution of an AGN component to the total $L_{\rm IR}$ as a function of the 6.2 μm EW of the sources. The dashed grey line corresponds to $f_{\rm AGN} = 0.5$.

and star-forming- dominated sources, with purely star-forming galaxies having $EW_{6.2} > 0.5$ μm.

To validate the classification based on the 6.2 μm PAH equivalent width we used the revised IRAC colour selection of Donley et al. (2012), which combines the AGN selection wedges (e.g., Lacy et al. 2004; Stern et al. 2005) with the infrared power-law selection of AGN (Alonso-Herrero et al. 2006; Donley et al. 2007; Park et al. 2010). This AGN selection limits the contamination by star-forming galaxies, and is also reliable for the identification of luminous AGNs (Mendez et al. 2013). We found that all but one of the sources in our sample with $EW_{6.2} > 0.2$ μm fail to meet the Donley et al. (2012) criteria, while ~80% of the sources with $EW_{6.2} \leq 0.2$ μm would be classified as AGN based on their IRAC colours (Fig. 1 left).

The plethora of mid-to-far-IR data that are available for our sample, and especially the IRS spectra, makes it possible to use a third classification of the sources based on the relative contribution of an AGN in the infrared output of our sample. For this task we use the AGN-host-galaxy decomposition method of Mullaney et al. (2011). This method employs a host-galaxy and an intrinsic AGN template SED to measure the contribution to the infrared output of these two components[2]. This technique identifies the best-fitting model SED to the observed infrared data (spectra and photometry) through χ^2 minimisation and by varying the values of a set of free parameters. In brief, these free parameters are: 1) the host-galaxy SED (a set of five templates); 2) the wavelength of the spectral break (if there is one) in the mid-IR SED of an AGN ($\lambda_{\rm brk}$); 3) the spectral indices (α_1 and α_2) below and above $\lambda_{\rm brk}$; 4) the wavelength at which the SED of the AGN component peaks; 5) the dust extinction of the AGN and host-galaxy component using a Draine et al. (2003) profile; and 6) the relative normalisations of the two components. Examples of the best model SEDs are shown in Fig. 2.

From the various output parameters here we focused on the recovered $L_{\rm IR}$ and the contribution of an AGN in the total infrared output ($f_{\rm AGN}$). The SED decomposition can only trace possible misidentifications of AGN as star-forming galaxies, but not the other way round. Indeed, if our classification is correct, then the majority of the bolometric IR output of a star-formation-dominated galaxy cannot be due to AGN activity. On the other hand, a strong AGN that dominates the mid-IR spectrum does not necessarily also dominate the total energy output of the source. With this in mind, we plot in Fig. 1 (right) the AGN fraction that corresponds to the best fit as a function of $EW_{6.2}$. We found that sources with $EW_{6.2} > 0.2$ μm tend to have, on average, a lower contribution of an AGN to their IR output, confirming the validity of our classification as star-forming dominated sources. In contrast, all sources for which we inferred that more than 50% of the total $L_{\rm IR}$ arises from dust heated by an AGN have $EW_{6.2} \leq 0.2$ μm and the majority of them are found to meet the IRAC colour criteria of Donley et al. (2012) (Fig. 1 left). We also note that while for 60% of the sources with $EW_{6.2} > 0.2$ μm the best-fit yields a non-zero AGN contribution, based on the Akaike information criterion (Akaike 1974), a solution without the need of an AGN component is equally probable within a 68% confidence interval for 80% of them. On the other hand, for almost all sources (95%) with $EW_{6.2} < 0.2$ μm, the existence of an AGN is favoured at a $>5\sigma$ confidence level.

Given the very good agreement between the three independent indicators, we conclude that the EW of the 6.2 μm feature is a reliable tool, at least for our sample, for identifying AGN versus star-formation-dominated sources. Based on the $EW_{6.2}$ classification, our sample consists of 116 SF and composite galaxies (70%), and 50 AGN-dominated sources (30%). While we did not find a trend between $f_{\rm AGN}$ and $EW_{6.2}$ in the $EW_{6.2} > 0.2$ μm regime, for consistency with previous works in the literature we will refer to galaxies with 0.2 μm $< EW_{6.2} \leq 0.5$ μm as composite and to galaxies with $EW_{6.2} > 0.5$ μm as star-forming.

3. Analysis

Several key physical properties of distant galaxies, such as infrared luminosities ($L_{\rm IR}$), dust temperatures ($T_{\rm d}$) and dust masses ($M_{\rm dust}$), can be estimated by fitting their mid-to-far-IR SEDs with various models and templates. However, the lack of sufficient data for a proper characterisation of the SED has often limited this kind of analysis to models suffering from over-simplified assumptions and broad generalisations. The *Spitzer*

[2] We uses the DECOMPIR routine, available at https://sites.google.com/site/decompir/

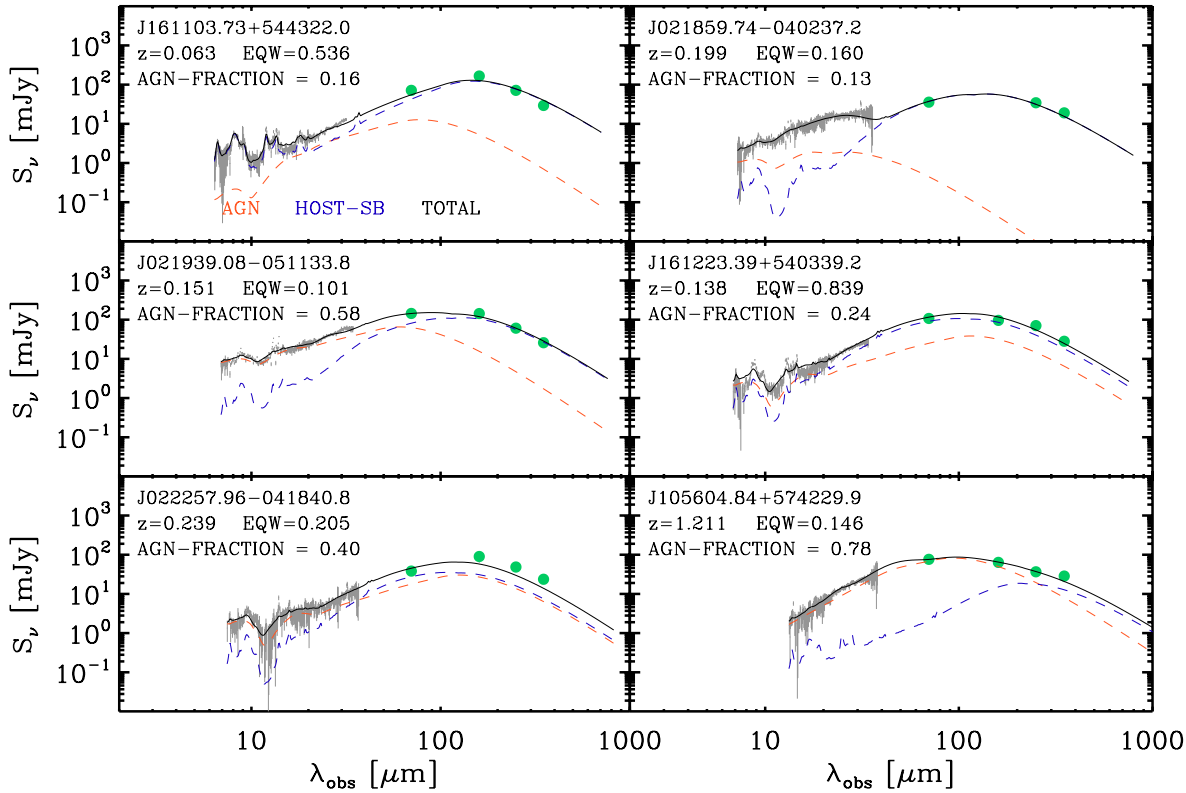


Fig. 2. Examples of SED fitting using the AGN/host-star-forming galaxy decomposition technique of Mullaney et al. (2011). Green circles are the observed points, overlaid with the best-fit total model (black line). The AGN and host galaxy components are shown as red and blue dashed lines, respectively.

and *Herschel* data available for the galaxies in our sample provide thorough photometric sampling of their SEDs, allowing the use of more realistic models of the sort that have previously been applied mainly in the analysis of nearby galaxies. Here, we considered both the physically motivated Draine & Li (2007, hereafter DL07) models for non-AGN-dominated sources and the more simplistic, but widely used, modified blackbody model (MBB) for the whole sample.

3.1. Draine & Li 2007 model

We employed the dust models of DL07, which constitute an update of the models developed by Weingartner & Draine (2001) and Li & Draine (2001). These models describe the interstellar dust as a mixture of carbonaceous and amorphous silicate grains, whose size distributions are chosen to mimic the observed extinction law in the Milky Way (MW), the Large Magellanic Cloud (LMC), and the Small Magellanic Cloud (SMC) bar region. The properties of these grains are parameterised by the PAH index, $q_{\rm PAH}$, defined as the fraction of the dust mass in the form of PAH grains. The majority of the dust is heated by a radiation field with a constant intensity $U_{\rm min}$, while a smaller fraction γ of the dust is exposed to a power-law distribution of star light intensities extending from $U_{\rm min}$ to $U_{\rm max}$. The $U = U_{\rm min}$ component can be interpreted as the dust in the general diffuse ISM, while the power-law starlight distribution allows for dust heated by more intense starlight, such as in the intense PDRs in star-forming regions. For simplicity, emission from dust heated by $U > U_{\rm min}$ is referred to as the PDR, or the warm dust component, and the emission from dust heated by $U = U_{\rm min}$ is referred to as the diffuse ISM or the cold dust component. Although the PDR component contains only a small fraction of the total dust mass, in some galaxies it contributes a substantial fraction of the total power radiated by the dust. Then, according to DL07, the amount of dust, $\mathrm{d}M_{\rm dust}$, exposed to radiation intensities between U and $U + \mathrm{d}U$, can be expressed as a combination of a δ-function and a power law:

$$\frac{\mathrm{d}M_{\rm dust}}{\mathrm{d}U} = \{(1-\gamma)M_{\rm dust}\delta(U-U_{\rm min}) + \gamma M_{\rm dust}\frac{\alpha-1}{U_{\rm min}^{1-\alpha}-U_{\rm max}^{1-\alpha}}U^{-\alpha}, \quad (1)$$

with $U_{\rm min} \leq U_{\rm max}, \alpha \neq 1$). Here, U is normalised to the local Galactic interstellar radiation field, $M_{\rm dust}$ the total dust mass, α the power-law index, γ the fraction of the dust mass that is associated with the power-law part of the starlight intensity distribution, and $U_{\rm min}$, $U_{\rm max}$ and α characterise the distribution of starlight intensities in the high-intensity regions.

Following DL07, the spectrum of a galaxy can be described by a linear combination of one stellar component approximated by a blackbody with colour temperature $T_* = 5000$ K, and two dust components, one arising from dust in the diffuse ISM, heated by a minimum radiation field $U_{\rm min}$ (diffuse ISM component), and one from dust heated by a power-law distribution of starlight, associated with the intense photodissociation regions (PDR component). Then, the model emission spectrum of a galaxy at distance D is:

$$f_\nu^{\rm model} = \Omega_* B_\nu(T_*) + \frac{M_{\rm dust}}{4\pi D^2} \times \left[(1-\gamma)p_\nu^{(0)}(q_{\rm PAH}, U_{\rm min}) + \gamma p_\nu(q_{\rm PAH}, U_{\rm min}, U_{\rm max}, \alpha)\right], \quad (2)$$

where Ω_* is the solid angle subtended by stellar photospheres, $p_\nu^{(0)}(q_{\rm PAH}, U_{\rm min})$, and $p_\nu(q_{\rm PAH}, U_{\rm min}, U_{\rm max}, \alpha)$ are the emitted

power per unit frequency per unit dust mass for dust heated by a single starlight intensity $U_{\rm min}$, and dust heated by a power-law distribution of starlight intensities for $\mathrm{d}M/\mathrm{d}U \propto U^{-\alpha}$ extending from $U_{\rm min}$ to $U_{\rm max}$.

In principle, the dust models in their most general form are dictated by seven free parameters, (Ω_*, $q_{\rm PAH}$, $U_{\rm min}$, $U_{\rm max}$, α, γ and $M_{\rm d}$). However, Draine et al. (2007) showed that the overall fit is insensitive to the details of the adopted dust model (MW, LMC, and SMC) and the precise values of α and $U_{\rm max}$. These authors showed that fixed values of $\alpha = 2$ and $U_{\rm max} = 10^6$ successfully describe the SEDs of galaxies with a wide range of properties. Draine et al. 2007 also favour the choice of MW dust properties for which a set of models with $q_{\rm PAH}$ ranging from 0.4% to 4.6% is available. Furthermore, because low $U_{\rm min}$ values correspond to dust temperatures below ~15 K that cannot be constrained by far-IR photometry alone, in the absence of rest-frame (sub)mm data ($\lambda_{\rm rest} = 850$ μm), the authors using $0.7 \leq U_{\rm min} \leq 25$. While this lower cutoff for $U_{\rm min}$ prevents the fit from converging to erroneously large amounts of cold dust heated by weak starlight ($U_{\rm min} < 0.7$), the caveat is a possible underestimate of the total dust mass if large amounts of cold dust are indeed present. However, Draine et al. (2007) concluded that omitting rest-frame (sub)mm data from the fit increases the scatter of the derived masses to up to 50% but does not introduce a systematic bias in the derived total dust masses.

Under these assumptions, we fit the broadband *Spitzer* and *Herschel* data of each galaxy with $EW_{6.2} > 0.2$ μm in our sample, searching for the best-fit model by χ^2 minimisation and parametrising the goodness of fit by the value of the reduced χ^2, $\chi^2_\nu \equiv \chi^2/N_{\rm dof}$ (where $N_{\rm dof}$ is the number of degrees of freedom). To further exploit the available information provided by the IRS spectra, for each source we estimated the observed flux density at 16 μm as it would be measured with the 16 μm IRS peak-up image, and at 30 μm assuming a 2 μm wide top-hat filter[3].

The best-fit model yields a total dust mass ($M_{\rm dust}$), $U_{\rm min}$, as well as γ and $q_{\rm PAH}$, while to derive $L_{\rm IR}$[4] estimates we integrated the emerging SEDs from 8 to 1000 μm:

$$L_{\rm IR} = \int_{8\ \mu\mathrm{m}}^{1000\ \mu\mathrm{m}} L_\nu(\lambda) \times \frac{c}{\lambda^2}\,\mathrm{d}\lambda. \quad (3)$$

A by-product of the best-fit model is also the dust-weighted mean starlight intensity scale factor, $\langle U \rangle$, defined as

$$\langle U \rangle = \frac{L_{\rm dust}}{P_0 M_{\rm dust}}, \quad (4)$$

where P_0 is the power absorbed per unit dust mass in a radiation field with $U = 1$. Note that $\langle U \rangle$ is essentially proportional to $L_{\rm IR}/M_{\rm dust}$, and for the definition of $L_{\rm IR}$ adopted here, that is, L_{8-1000}, Magdis et al. (2012b) have shown that $P_0 \approx 125$.

Uncertainties in $L_{\rm IR}$ and $M_{\rm dust}$ were quantified using Monte Carlo simulations. To summarise, for each galaxy a Gaussian random number generator was used to create 1000 artificial flux sets from the original fluxes and measurement errors. These new data sets were then fitted in the same way, and the standard deviation in the new parameters was taken to represent the uncertainty in the parameters found from the real data set. Examples of the best-fit DL07 models along with the observed photometric points are shown in Fig. 3, while the set of best-fit parameters for each source are given in Table 2. We note that the DL07 models are representative of star-formation-dominated galaxies or equally for sources that do not harbour a strong AGN. As a consequence, our analysis was restricted to star-formation dominated galaxies. For AGN-dominated sources in our sample (i.e., $EW_{6.2} \leq 0.2$ μm) we adopted the $L_{\rm IR}$ measurements derived by the SED decomposition described in the previous section.

3.2. Comparison with modified blackbody fits

Another method for deriving estimates of the dust properties is to fit the far-IR to submm SED of the galaxies with a single-temperature modified blackbody (MBB), expressed as

$$f_\nu \propto \frac{\nu^{3+\beta}}{\mathrm{e}^{\frac{h\nu}{kT}} - 1}, \quad (5)$$

where T is the effective dust temperature ($T_{\rm d}$) and β is the effective dust emissivity index. Then, from the best-fit model, one can estimate $M_{\rm dust}$ from the relation

$$M_{\rm dust} = \frac{S_\nu D_L^2}{(1+z)\kappa_{\rm rest} B_\nu(\lambda_{\rm rest}, T_d)}, \quad \text{with} \quad \kappa_{\rm rest} = \kappa_0 \left(\frac{\lambda_o}{\lambda_{\rm rest}}\right)^\beta, \quad (6)$$

where S_ν is the observed flux density, D_L is the luminosity distance, and $\kappa_{\rm rest}$ is the rest-frame dust mass absorption coefficient at the observed wavelength. While this is a simplistic approach, mainly adopted due to the lack of sufficient sampling of the SED of distant galaxies, it has been one of the most widely used methods in the literature. Therefore, an analysis based on MBB-models provides both estimates of the effective dust temperature of the galaxies in our sample, a quantity that is not directly measured from the DL07 model, and a valuable comparison between dust masses inferred with the MBB and DL07 methods. We note that unlike the DL07 analysis, which is restricted to non-AGN sources, the MBB technique and the derived $T_{\rm d}$ measurements, are also valid for AGN-dominated sources.

We fit the standard form of a modified blackbody considering observed data points with $\lambda_{\rm rest} > 60$ μm, to avoid emission from very small grains, and used a fixed value of $\beta = 1.5$, typical of star-forming galaxies (Hildebrand 1983; Gordon et al. 2010; Magdis et al. 2011b; Dale et al. 2012). From the best fit model, we then estimated the total $M_{\rm dust}$ with equation 6, considering all sources, including AGN, with at least three available photometric points at $\lambda_{\rm rest} > 60$ μm. For consistency with the DL07 models we adopted a value of $\kappa_{250} = 5.1$ cm^2 g^{-1} (Li & Draine 2001). To obtain the best-fit models and the corresponding uncertainties of the parameters, we followed the same procedure as for the DL07 models. The derived parameters are summarised in Table 2 and the best-fit models are shown in Fig. 3.

A comparison between dust masses derived by DL07 and MBB is shown in Fig. 4. We see that the modified blackbody technique yields dust masses that are lower than those derived based on DL07 models on average by a factor of ~2 ($\langle M_{\rm dust}^{\rm DL07}/M_{\rm dust}^{\rm MBB}\rangle = 2.13 \pm 0.36$)[5]. This result agrees with Magdis et al. (2012b) for a sample of $z \sim 1$–2 star-forming galaxies and Dale et al. (2012), who found that the discrepancy between the two dust mass estimates increases for sources with lower S_{70}/S_{160} ratios that correspond to colder dust temperatures. This is caused by the inability of the single-temperature models to account for the wide range in the temperature of dust grains that

[3] We chose to measure the flux density at 30 μm since beyond that wavelength the IRS spectra become progressively more noisy, as a result of the delimitation of the first-order long-low module filter.

[4] $L_{\rm dust}$ quoted below is similar to $L_{\rm IR}$, but integrated from 0 to ∞.

[5] Fixing $\beta = 2$, returns dust masses that are larger than those inferred when $\beta = 1.5$, by a factor of ~1.2 but still lower by a factor of ~1.8 than the masses derived by DL07.

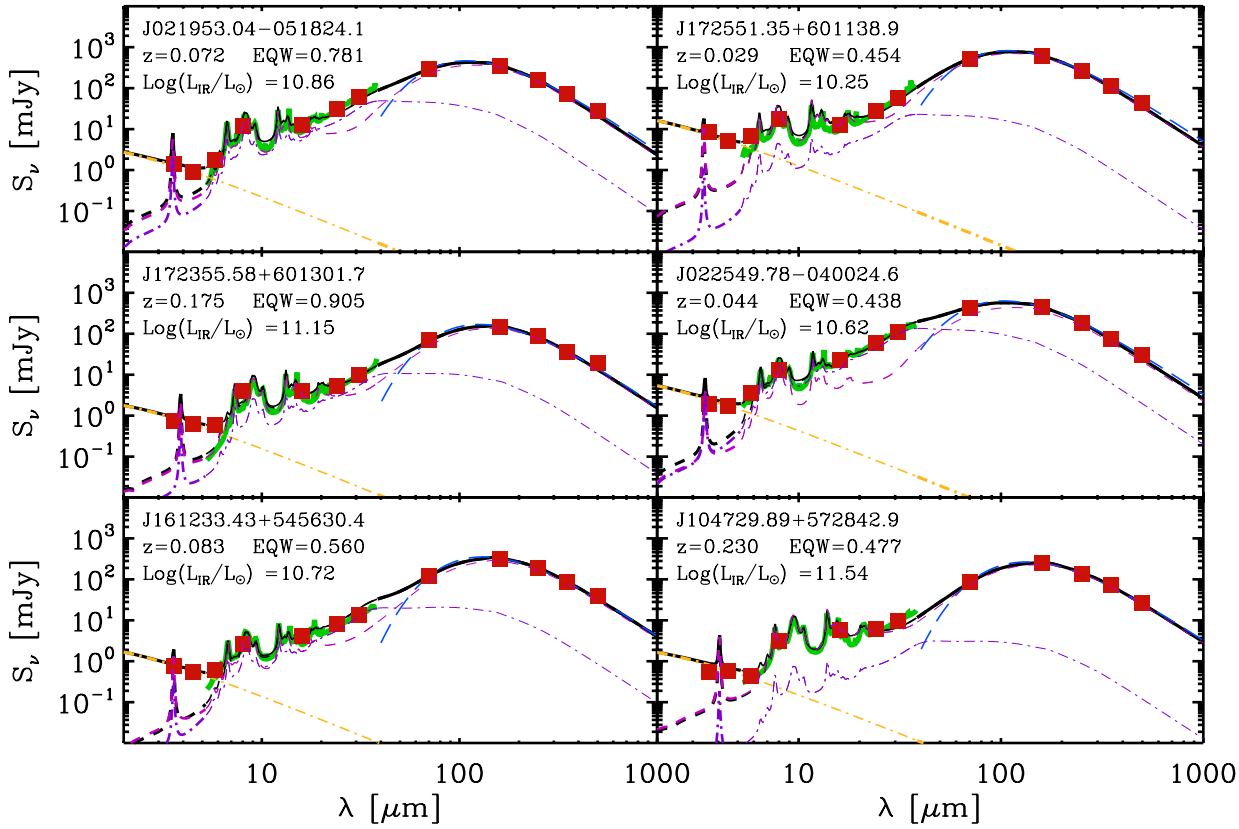


Fig. 3. Examples of SED fitting. Red squares are observed points, overlaid with the best-fit DL07 model (black line). The PDR and diffuse ISM components are shown in purple. The yellow line is the stellar component and the dashed blue line the best-fit modified blackbody model with $\beta = 1.5$. The green line in the mid-IR is the actual IRS spectrum of each source. We convolved the observed IRS spectrum with the IRS 16 μm peak-up imaging filter and a 2 μm-wide top-hat filter centred at observed 30 μm to enhance our fit with two more points in the observed mid-IR part of the spectrum. The rest of the data are taken from IRAC, MIPS, and SPIRE.

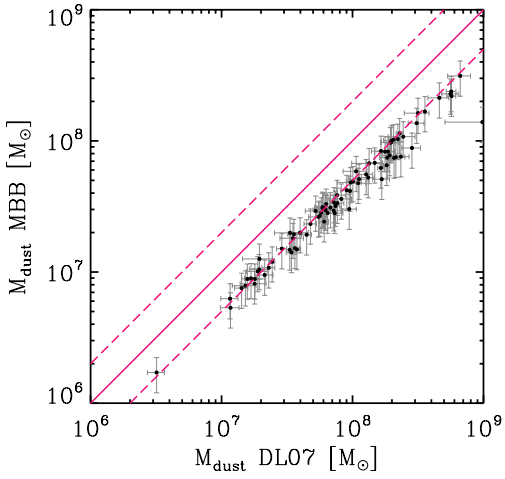


Fig. 4. Comparison between dust masses derived based on a single-temperature modified blackbody (MBB) and masses derived using the Draine & Li (2007) models. For the MBB derived $M_{\rm dust}$ we assume $\beta = 1.5$. The purple solid line corresponds to unity and the two purple dashed lines to its offset by a factor of 2 and 0.5.

are exposed to different intensities of the interstellar radiation field. Fitting simultaneously both the Wien side of the modified black-body (which is dominated by warm dust), as well as the Rayleigh-Jeans tail (sensitive to colder dust emission) drives the derived temperatures to higher values and consequently to lower dust mass estimates (e.g. Dunne et al. 2000). On the other hand, a more physically motivated two-temperature blackbody fit returns dust masses that are larger by a factor of ~2 compared with those derived based on a single $T_{\rm d}$ MBB (Dunne & Eales 2001), in agreement with those inferred by the DL07 technique. For the rest of our analysis we only consider $M_{\rm dust}$ estimates derived based on the DL07 model.

3.3. Comparison with Spitzer L_{IR} measurements

In the pre-*Herschel* era the infrared properties of the 5MUSES sample were constrained based on *Spitzer* IRAC, IRS, and MIPS data. In particular, for the redshift range of the majority of the sources, the 70 μm and 160 μm MIPS bands traced the emission of the galaxies on both sides of the peak of the SED, providing a first insight into the overall shape of their SEDs in the far-IR and their $L_{\rm IR}$ values. However, only half of the sample is detected at 160 μm. Furthermore, in the absence of the sub-mm data, the shape of the Rayleigh-Jeans tail of the galaxies in the 5MUSES sample was largely unconstrained.

Here, we examined the impact of adding *Herschel* data to the derived $L_{\rm IR}$ estimates of the sample. In Fig. 5 we compare the $L_{\rm IR}$ measurements by Wu et al. (2010) based solely on *Spitzer* data (i.e., IRS and MIPS) with those derived in our study. The two estimates are in excellent agreement, with a mean ratio ($L_{\rm IR}^{Herschel}/L_{\rm IR}^{Spritzer}$) of 0.98 and a standard deviation of 0.22. This is in line with various studies that have shown that mid-IR extrapolations of the total $L_{\rm IR}$ are correct for star-forming galaxies at $z < 1.5$ (e.g., Elbaz et al. 2010; Rodighiero et al. 2010). We stress that only nine sources in our sample lie at $z > 1.5$, while ~90% of the 5MUSES sample considered here are at $z < 0.5$. The very good agreement between the

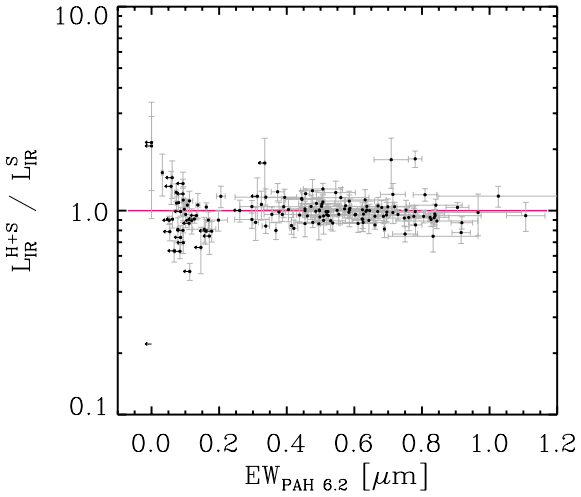


Fig. 5. Ratio of the total IR luminosity (L_{IR}) estimated using both *Herschel* and *Spitzer* data (L_{IR}^{H+S}) over the one using only *Spitzer* (L_{IR}^{S}, see Wu et al. 2010) as a function of the $EW_{6.2}$. (see Sect. 3.3). The solid purple line corresponds to the 1−to−1 relation between the two L_{IR} estimates.

two estimates also holds when we consider the three different classes of sources individually (starbursts, composite and AGN-dominated) although, we notice a somewhat larger discrepancy for the AGN-dominated sources, with $(L_{IR}^{Herschel}/L_{IR}^{Spitzer}) = 0.90 \pm 0.35$, compared with 1.01 ± 0.16 and 0.99 ± 0.16 for composite and starburst galaxies, respectively. Finally, we note that the addition of *Herschel* submm data has a noticeable impact on the corresponding uncertainties of the measured L_{IR}, which are reduced by a factor of about 3.

4. Mid- to far-IR properties of AGN and star-forming galaxies

The detailed mid-to-far-IR SEDs of our sample, as traced both by IRS spectroscopy and *Spitzer* and *Herschel* broadband photometry, allows for an in-depth investigation of the total infrared spectra for our sample. In this section we study possible correlations between mid-IR spectral features, and warm and cold dust components as well as variations of the PAH features between star-forming and AGN-dominated galaxies.

4.1. Warm and cold dust

The wide range in the 6.2 μm EWs in our sample reveals a variety of mechanisms that power the warm dust emission, ranging from purely star-forming galaxies to AGN-dominated sources. The impact of an AGN on the broadband mid-IR photometry is known to be prominent, with AGN-dominated sources exhibiting shallower mid-IR spectral slopes. For example, Wu et al. (2010) reported that while composite and SF sources share very similar S_{30}/S_{15} (and S_{70}/S_{24}) flux density ratios, AGN-dominated sources are clearly separated from the rest with considerably lower S_{30}/S_{15} (and S_{70}/S_{24}) values. With the addition of the *Herschel* data we are now in a position to advance this investigation by studying variations of the warm to cold dust emission among the different classes, and to infer the impact of an AGN on the total infrared emission of the galaxies.

We first investigated the L_{24}/L_{IR} ratio of our sources, where L_{24} is the rest-frame 24 μm luminosity as measured from the rest-frame IRS spectra of the galaxies. This ratio can serve as an indicator of the contribution of the warm emission to the total IR output of a galaxy, or equally to the relative amount of warm (L_{24}) to total (L_{IR}) dust mass. As shown in Fig. 6 (left), AGN tend to exhibit an enhanced L_{24}/L_{IR} ratio compared with that of star-forming galaxies. We notice, however, that within each group (AGN, composites and star-forming galaxies) we find no correlation between L_{24}/L_{IR} and $EW_{6.2}$. Instead, the L_{24}/L_{IR} remains roughly constant within each group, albeit with a considerable scatter. In particular, we found a mean value and a standard deviation of $\langle L_{24}/L_{IR}\rangle = 0.14 \pm 0.04$ for star-forming galaxies, 0.17 ± 0.08 for composites, and 0.32 ± 0.09 for AGN-dominated sources. Evidently, the relative amount of warm dust in AGN as traced by the L_{24}/L_{IR} ratio is higher than that found in star-forming galaxies, revealing an additional mechanism, to the energetic photons produced by young stars, which heats the dust and boosts the mid-IR emission. Because the relative amount of warm dust in AGN-dominated sources is boosted by a factor of ∼3 (for this redshift range), it is natural to expect that a considerable fraction of the bolometric infrared luminosity would arise from AGN activity in these systems. Indeed, based on the SED decomposition presented in the previous section, we found that for 75% of the AGN with $L_{24}/L_{IR} > 0.3$, more than half of the emerging L_{IR} is powered by the AGN (see Fig. 6 left).

With the *Herschel* data in hand, we are also in a position to investigate whether the dominant powering mechanism, as traced by the spectral features in the mid-IR, has an impact on the cold dust emission. In Fig. 6 (middle), we plot the derived T_d measurements of the cold dust ($\lambda_{rest} > 60$ μm), as derived from the MBB fit, versus the 6.2 μm EW of the sources in our sample. It appears that the cold dust temperature remains roughly constant for the whole range of EWs, with only a small, statistically insignificant, increase in T_d as we move into the AGN regime. Indeed, composite and star-forming galaxies share similar dust temperatures with $\langle T_d\rangle = (31 \pm 3)$ K, while AGN-dominated sources are marginally, although consistent within the uncertainties, warmer with $\langle T_d\rangle = (34 \pm 4)$ K. The same trend is seen when we plot the dust temperature versus the fraction of L_{IR} that arises from AGN activity within the galaxy (Fig. 6 right). Sources for which the SED decomposition suggests that more than half of the total L_{IR} originates from AGN activity have $\langle T_d\rangle = (34 \pm 3)$ K, while for the rest we found $\langle T_d\rangle = (31 \pm 3)$ K. Hence, our analysis suggests that the far-IR part of the SED, as traced by the SPIRE bands in our sample, is predominantly shaped by, and directly linked to star formation and does not carry any measurable signature of AGN activity. This is in agreement with the findings of Hatziminaoglou et al. (2010), who reported that SPIRE colours, which are a good proxy of cold dust T_d, are almost indistinguishable between star-forming and AGN-dominated sources. We stress though that this applies to AGN-dominated sources in our sample for which it was feasible to derive a T_d estimate, that is, those that are luminous enough in the submm to be detected in the SPIRE bands. With this in mind, we conclude that while the cold dust emission as traced by the SPIRE bands does not reveal the presence of an AGN, there is a marked difference in the mid- to far-IR colours of star-forming and AGN dominated sources, yielding larger amounts of warm dust in the latter. We note that similar results were reached by Kirkpatrick et al. (2012b) and Sajina et al. (2012), based on samples of $z = 0.4$−5 galaxies.

As we have seen, the bolometric infrared output of galaxies with $EW_{6.2} > 0.2$ μm in our sample is dominated by star formation activity. Therefore, the derived parameters from the DL07 models provide meaningful constraints on the warm and cold dust emission. In Fig. 7(left) we explore the contribution of

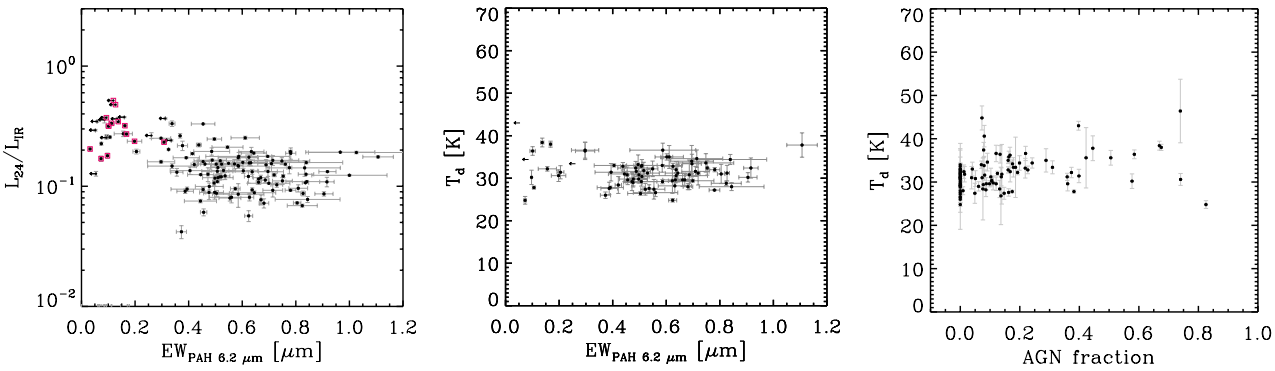


Fig. 6. *Left*: L_{24}/L_{IR} ratio as a function of the 6.2 μm PAH feature EW. Purple squares correspond to sources for which the SED decomposition suggests that the AGN contribution to the total L_{IR} is >50%. Leftward arrows denote upper limits in $EW_{6.2}$ measurements. *Middle*: T_d versus $EW_{6.2}$. T_d estimates are derived based on a modified blackbody model for 79 sources (out of the total 154 sources shown in *the left panel*), which are detected in at least three bands at $\lambda_{rest} > 60$ μm. *Right*: T_d versus fraction of L_{IR} arising from AGN activity, as derived based on SED decomposition.

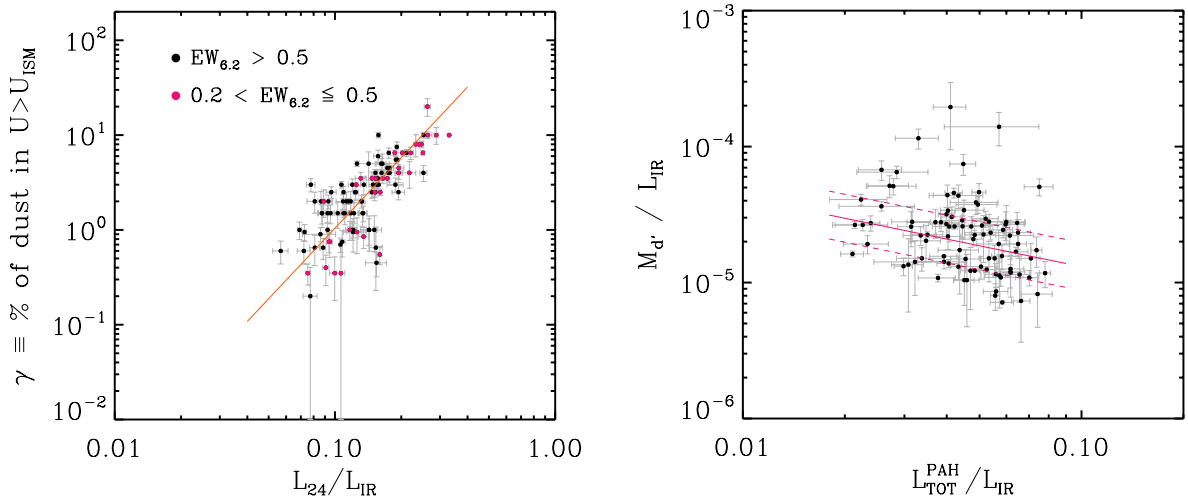


Fig. 7. *Left*: fraction of M_{dust} heated by radiation fields stronger than that of the diffuse ISM (or equivalently by $U > U_{min}$) as a function of the L_{24}/L_{IR} ratio for star-formation-dominated sources with $EW_{6.2} > 0.5$ μm (black circles) and 0.2 μm < $EW_{6.2} \leq 0.5$ μm (purple circles). The orange line depicts the best fit to the data. *Right*: dust mass heated by $U > U_{min}$ versus L_{TOT}^{PAH}. Both quantities are normalised by L_{IR}. The purple lines donate the best fit to the data and a scatter of 0.2 dex.

a PDR component to the infrared output, or in other words the fraction of dust heated by PDRs (γ), as a function of the warm to total dust emission ratio as traced by L_{24}/L_{IR}. We recall that the "PDR" component in the DL07 models describes the amount of dust exposed to starlight with intensities higher than U_{min}, which is the radiation field of the diffuse ISM. Both for the composite and for the star-forming galaxies, we found a correlation between the two quantities, with the fraction of L_{IR} that arises from PDRs increasing for galaxies with higher L_{24}/L_{IR} ratios, or equally for a larger portion of warm dust. Composite and star-forming galaxies follow the same trend and span the same L_{24}/L_{IR} range, pointing to a similar mechanism heating their dust.

In Fig. 7(right) we also investigate the variations of the relative contribution of the PAH features to the total L_{IR}, as a function of the dust heated by radiation fields stronger than U_{min}, that is, $\gamma \times M_{dust}$. Instead of looking at a particular PAH emission feature we chose to consider the total PAH emission (L_{TOT}^{PAH}) as inferred by the sum of the fluxes of the 6.2, 7.7, and 11.3 μm spectral features of our sources. We found for fixed L_{IR}, a weak anti-correlation ($\rho = -0.38$) with PAH emission that decreases with increasing amount of dust heated by stronger radiation fields. While this trend could serve as evidence for PAH destruction in sources with a larger portion of their total dust mass exposed to stronger radiation fields, enhanced extinction or higher continuum levels cannot be ruled out by this analysis. In the next subsection we attempt to tackle this question.

4.2. L_{IR}/L_8 versus PAH emission in star-forming galaxies

Recent studies based on *Herschel* data have revealed a scaling law for star-forming galaxies, relating the total IR luminosity, L_{IR}, to the broadband (as traced by the IRAC 8 μm filter) rest-frame 8 μm luminosity, L_8. In particular, Elbaz et al. (2011), showed that the 8 μm bolometric correction factor, $IR8 \equiv L_{IR}/L_8$, does not vary as a function of L_{IR} or redshift. Instead, IR8 exhibits a Gaussian distribution containing the vast majority of star-forming galaxies both locally and up to $z \sim 2.5$, centred on IR8 $\approx$ 4.9 and with a scatter of $\sigma \approx 2.5$. However, since L_8 probes emission both from the 7.7 μm complex and from the underlying continuum, it has been unclear whether the observed spread in the $L_{IR}-L_8$ plane is mainly driven by PAH or mid-IR continuum variations. Furthermore, the determination of L_8 in these studies has primarily been based on K-corrected broadband photometry obtained by using template SEDs. Here, given the

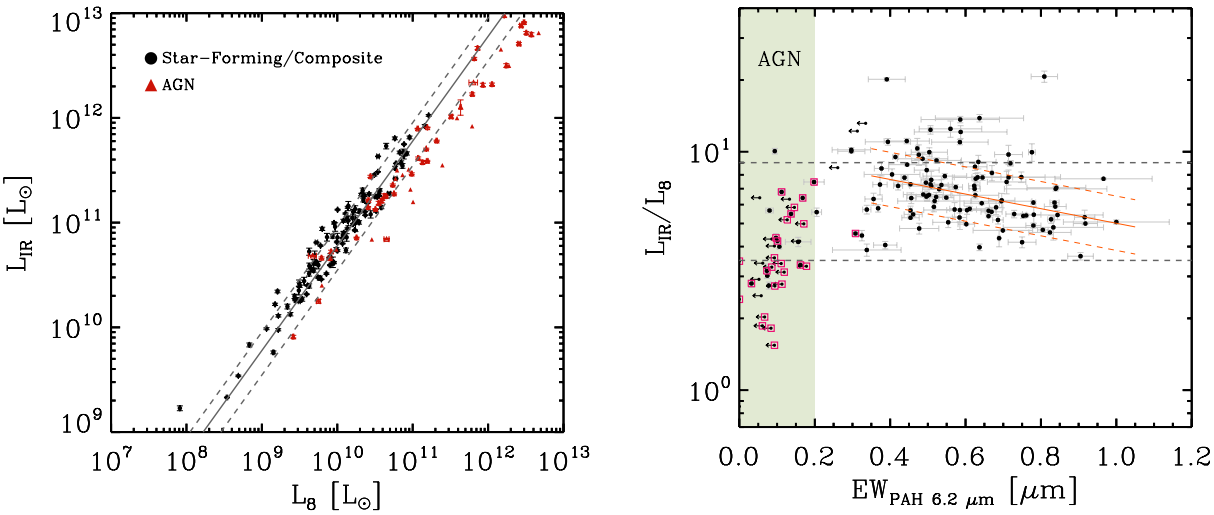


Fig. 8. *Left*: L_{IR} versus L_8 for the whole 5MUSES sample. Black circles correspond to purely star-forming and composite sources, while red triangles correspond to AGN. The solid grey line depicts the median and 68% dispersion of composite and star-forming galaxies. *Right*: L_{IR}/L_8 versus EW of 6.2 μm. The horizontal lines enclose the values of L_{IR}/L_8 within the 68% dispersion from the median. The orange lines depict the best-fit linear regression and its scatter in the $EW_{6.2} \geq 0.4$ μm regime. Purple squares correspond to sources with $f_{AGN} > 0.5$.

available IRS spectra, we can directly measure L_8, and in combination with the accurate L_{IR} estimates offered by the *Herschel* data, we can investigate the $L_{IR}-L_8$ relation among star-forming galaxies as well as for sources ranging from purely star-forming to AGN-dominated.

To estimate L_8 for each source in our sample we convolved its rest-frame IRS spectrum with the IRAC 8 μm filter. To account for possible flux losses due to the narrow IRS short-low slit we applied a correction factor estimated from the the ratio of the photometric (broad-band) over the synthetic (IRS) observed 8 μm (for sources with $z < 0.75$) and 24 μm (for $z > 0.75$) flux density. The overall correction is found to be on average <20%. The derived L_8 and L_{IR} measurements are shown in Fig. 8 (left). For star-forming and composite galaxies ($EW_{6.2} > 0.2$ μm), the two luminosities are found to correlate almost linearly (slope of ~0.97) with a median equal to IR8 = 6.0 $[-2.5, 2.9]$ in the whole range of L_{IR} (i.e. 10^9–10^{12} $L_\odot$). Interestingly, most of the AGN-dominated sources with $L_{IR} < 10^{11.5}$ $L_\odot$ also lie within the 68% scatter of the relation, in agreement with previous studies (e.g. Elbaz et al. 2011; Mullaney et al. 2012a; Kirkpatrick et al. 2012b). However, at higher luminosities (that also correspond to higher-redshift sources), the majority of AGN appear to deviate from the linear relation and exhibit an enhanced L_8 for their L_{IR}.

In Fig. 8, we explore the variation of IR8 as a function of the 6.2 μm equivalent width. We identified two trends: a mild increase in the IR8 as we move from purely star-forming to composite sources, and a dramatic drop when we enter the AGN regime ($EW_{6.2} < 0.2$ μm). In the $EW_{6.2} \geq 0.4$ μm regime a Spearman test yields a statistically significant ($p = 2.8 \times 10^{-5}$) anti-correlation ($\rho = -0.41$) between IR8 and $EW_{6.2}$. To examine whether this correlation is robust against the uncertainties associated with the $EW_{6.2}$ and IR8 values, we created 1000 realisations by allowing the data to take values selected from Gaussians (given the measured values and errors) and repeated the correlation ranking test. The mean and standard deviation of the derived correlations are $\rho = -0.39 \pm 0.09$, suggesting a weak but statistically significant anti-correlation between the two parameters.

Interestingly, this trend is not driven by L_{IR} because in this regime ($EW_{6.2} > 0.2$ μm), we found that IR8 and $EW_{6.2}$ do not correlate with L_{IR}. Since the $EW_{6.2}$ is an indicator of the strength of the 6.2 μm line relative to the underlying continuum, we examined whether this behaviour could be driven by variations of the 6.2 μm PAH features or by variations of the mid-IR continuum level. For a fixed L_{IR}, L_8 would increase if the drop in the $EW_{6.2}$ had been caused due to an elevated continuum, and hence IR8 would remain constant or even drop. Therefore, the decrease in $EW_{6.2}$ for star-forming galaxies is more likely to be due to lower PAH emission relative to L_{IR}, rather than an elevated 8 μm continuum emission. On the other hand, the sharp decrease of IR8 at $EW_{6.2} < 0.2$ μm, can be understood as an increase in the mid-IR continuum that results in both higher L_8 and lower $EW_{6.2}$ for a given L_{IR}.

To explore this scenario we split the sources into two bins of $EW_{6.2}$, 0.4 μm $\leq EW_{6.2} \leq$ 0.6 μm and $EW_{6.2} > 0.7$ μm. We then constructed a median IRS spectrum for each bin by stacking the individual spectra normalised to $L_{IR} = 1$ $L_\odot$. To ensure that the rest-frame 5 μm emission was traced by the IRS spectra we placed a lower limit of $z = 0.07$ on the redshift of the sources that enter the stack. For each spectrum we also define a local continuum or plateau below the PAH features by fitting the PAH features with Drude profiles using PAHFIT as described in Smith et al. (2007). The resulting spectra in the rest-frame 5–11 μm wavelength range and the corresponding continuum levels are shown in Fig. 9 (left). The two spectra exhibit almost identical continua at 6.2 μm with a noticeable difference in the emission of the PAH feature. This implies that for fixed L_{IR}, a decrease in the $EW_{6.2}$ of star-forming galaxies is primarily caused by a decrease in the emission of the 6.2 μm PAH feature and not by dilution from an elevated continuum emission in the 5–15 μm regime. On the other hand, the mean IRS spectrum of AGN dominated sources ($EW_{6.2} \leq 0.2$ μm) normalised to $L_{IR} = 1$ $L_\odot$ exhibits a mid-IR continuum about 10 times higher than that of the star-forming galaxies, suggesting that the decrease in IR8 is due to PAH destruction or smearing from the strong continuum emission. We note that repeating the analysis using a spline function does not change our result.

The mean spectra in various $EW_{6.2}$ bins also provide clues about the apparent increase of IR8 with decreasing $EW_{6.2}$ among star-forming galaxies. As shown in Fig. 9 (left), L_8 probes both

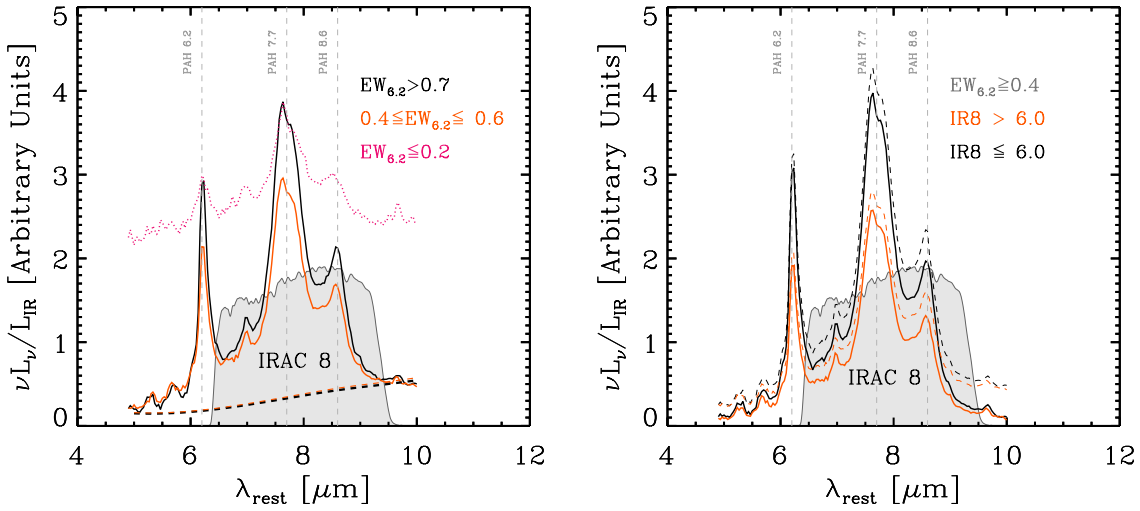


Fig. 9. *Left*: average spectra in various $EW_{6.2}$ bins in the 4−10 μm range. The dashed lines correspond to the underlying continuum emission as inferred by PAHFIT. The grey shadowed area depicts the 8.0 μm IRAC filter. *Right*: average (dashed lines), and average continuum subtracted (solid lines) spectra of of all galaxies with $EW_{6.2} \geq 0.4$ μm grouped in those with IR8 > 6 (orange lines), and IR8 < 6 (black lines).

the 7.7 μm PAH complex and the continuum emission arising from hot dust. Since the presented spectra are normalised to the same $L_{\rm IR}$ we can directly infer that at fixed $L_{\rm IR}$, sources with higher $EW_{6.2}$ have higher L_8 and hence, lower IR8. Indeed, measuring L_8 directly from the spectra yields an IR8 value for the sources in the 0.4 μm $\leq EW_{6.2} \leq$ 0.6 μm bin higher by a factor of ∼1.4 than to those with $EW_{6.2} \geq 0.7$ μm. The variation of the PAH features as a function of IR8 is more directly seen when we split our sample of star-forming galaxies into two IR8 bins, above and below IR8 = 6.0. The continuum-subtracted average IRS spectra of the two sub-samples are presented in Fig. 9 (right), clearly demonstrating a decrease of the PAHs emission for sources in the high IR8 bin. Indeed, the emission from the PAH features measured directly from the stacked spectra is higher by a factor of ∼1.5 in the low IR8 bin than that in the high IR8 bin.

We also investigated whether this result could be an artefact because different galactic scales are probed by the IRS at different redshifts. The low-z cutoff that we introduced in the stack ensures that the smallest galaxy scale traced by IRS is ∼6 kpc. Therefore, because we only probe a fraction of the disk for the low-z sample, we could indeed be missing extended PAH emission (e.g. Pereira-Santaella et al. 2010; Diaz-Santos et al. 2010b). An indication for the maximum of the PAH emission that we might be missing is given by the ratio of the broad-band (which traces the whole galaxy) to spectral flux ratio. As discussed above, this is only at a ∼15% level and therefore, our result would still hold because the observed PAH variation is of a factor of ∼1.5. We note though that this extreme scenario is unlikely to be the case because we would also see a correlation between the 6.2 μm EW (or IR8) and redshift. The absence of this correlation (as indicated from our data), suggests that the missed flux cannot originate solely from PAHs. Furthermore, Elbaz et al. (2011) and Diaz-Santos (2011) have shown that sources with higher IR8 exhibit more extended 11.3 μm PAH emission. Accordingly, one would expect that PAH emission is more likely to be missed for sources with lower IR8 values, which would additionally strengthen our result. Finally, repeating the analysis without applying any correction to L_8 yields the same results, albeit with an increase of the mean IR8 from 6.0 to 6.2. In summary, we have provided evidence that the spread in IR8 values of star-forming galaxies mirrors variations in their PAH emission. In the next section we discuss possible explanations for the origin of this observation.

5. Discussion

We have seen that the dispersion in the $L_{\rm IR}-L_8$ relation defined by star-forming galaxies traces variations in the PAHs emission with respect to $L_{\rm IR}$. Because the $L_{\rm IR}/L_8$ and $L_{\rm IR}/L_{\rm PAH}$ do not appear to correlate with $L_{\rm IR}$ (see also Wu et al. 2010), other physical parameters must drive this variation.

A possible explanation could be a varying level of AGN activity. However, there are several arguments against this scenario. First, for almost all sources with $EW_{6.2} \geq 0.4$ μm the SED decomposition allocates the bulk of $L_{\rm IR}$ to star-formation activity and none of them meet the power-law AGN criterion of Donley et al. (2012), known to be a reliable selection of AGN (Mendez et al. 2013). A prominent AGN activity would also boost L_8 and therefore decrease IR8 for a given $L_{\rm IR}$. This becomes clear in the $EW_{6.2} < 0.2$ μm regime, where almost all sources are selected as power-law AGNs and, as stated above, lie in the lower regime of the IR8 main sequence or fall below it. Finally, as shown in Fig. 1(right), we do not observe any correlation between $EW_{6.2}$ and contribution of an AGN to the total $L_{\rm IR}$. This means that the observed increase of IR8 with decreasing $EW_{6.2}$ cannot be explained by an increasing AGN activity.

An alternative scenario that could explain the variation of the PAH strength among star-forming galaxies is a variation in the hardness of the interstellar radiation field (U). As argued by Abel et al. (2009), under the assumption of a constant gas density, an increase in U and therefore of the number of ionising photons ($h\nu > 13.6$ eV) produced by young, massive, OB stars, would lead to an increase of the ratio of ionised to atomic hydrogen and consequently to a reduced gas opacity. As U increases, the H II regions extend to higher A_V into the cloud, and a larger portion of the UV photons are absorbed by the dust in the ionised region and are re-emitted in the form of IR emission. The net effect is that the fraction of UV photons available to ionise or excite the PAH molecules in the surrounding PAH-rich PDRs or in the neutral ISM is reduced for higher U values, resulting in lower PAH emission for a fixed $L_{\rm IR}$ (e.g. Peeters et al 2004). In this scenario one would expect an anti-correlation between the strength of the PAHs relative to the continuum emission and the

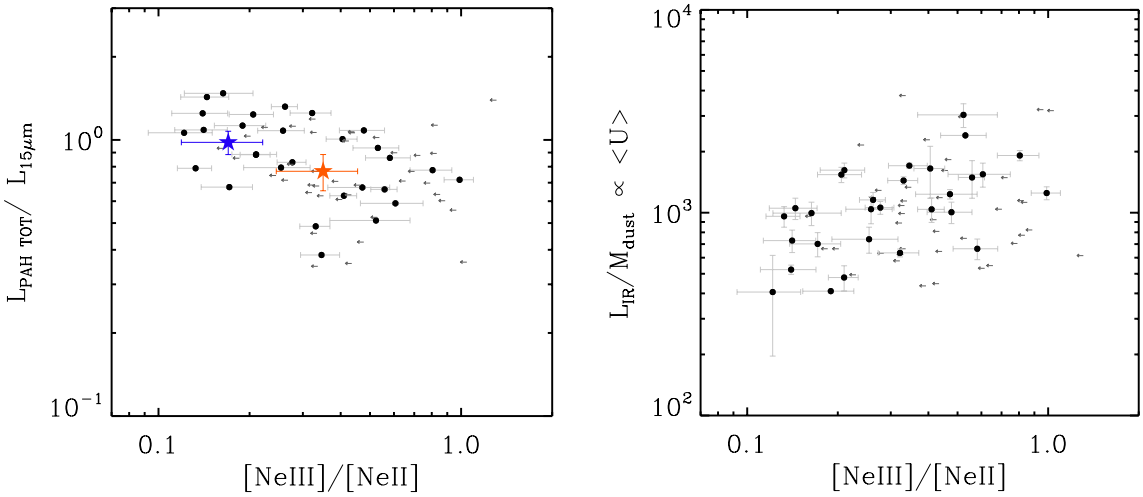


Fig. 10. *Left*: L_{TOT}^{PAH}/L_{15} versus [Ne III]/[Ne II], as measured from the IRS spectra of the sources in our sample with $EW_{6.2} \geq 0.4$ μm. The orange and blue stars correspond to the average spectra of galaxies with IR8 $\leq$ 6.0 and 6.0 < IR8 < 9.0, respectively. Leftward arrows denote upper limits of the [Ne III]/[Ne II] ratio for sources with only a [Ne II] detection *Right*: dust-mass-weighted luminosity (L_{IR}/M_{dust}) as a function of the hardness of the radiation field traced by the [Ne III]/[Ne II] line ratio.

hardness of the radiation field. This has already been shown to be the case in various samples of local galaxies and star-forming regions in the local Universe (e.g. Peeters et al. 2002; Madden et al. 2006; Wu et al. 2006).

To test this scenario we considered the ratio of [Ne III] λ15.56 μm and the [Ne III] λ12.81 μm lines, which is a common tracer of the hardness of the radiation field (e.g. Genzel et al. 1998; Madden et al. 2006; Farrah et al. 2007). The diagnostic value of this ratio is based on 1) the large difference in the ionisation potential of the Ne^{++}(41 eV) and Ne^{+}(21.6 eV); 2) the fact that this ratio is independent of the neon abundances; and 3) does not suffer from differential extinction due to the proximity of the wavelength of the two emitted lines. In Fig. 10 (left) we plot the L_{TOT}^{PAH}/L_{15} as a function of [Ne III]/[Ne II] for galaxies in our sample with $EW_{6.2} \geq 0.4$ μm and for which the two lines have been detected. The anti-correlation between the strength of the radiation field and the relative strength of the PAH seen in previous studies of local galaxies appears to hold for our sample, too, suggesting that galaxies with harder radiation fields, as traced by the [Ne III]/[Ne II] line ratio, tend to exhibit weaker PAH emission than the underlying continuum. In this scenario the PAH deficit could originate from PAH destruction from energetic photons produced by young and massive stars.

We also measured the [Ne III]/[Ne II] ratio from the stacked spectra in the two IR8 bins (IR8 < 6.0 and 6.0 < IR8 < 9.0) and found that galaxies with higher IR8 values have a mean [Ne III]/[Ne II] (and L_{TOT}^{PAH}/L_{15}) ratio that is approximately a factor of ~2 higher than that of galaxies with IR8 < 6.0. We note, however, that there is only a very weak trend between IR8 and [Ne III]/[Ne II] in individual detections. To explain this lack of a clear correlation between IR8 and [Ne III]/[Ne II] we recall that [Ne III]/[Ne II] might mirror variations in the age of the starburst (e.g. Thornley et al. 2000). It is possible that galaxies with higher [Ne III]/[Ne II] ratios have experienced a more recent (up to 2 Myrs) starburst event with a larger fraction of young and massive OB stars than older starbursts. Therefore, the mid-IR fine structures lines (those of neon in our case) predominantly trace the youngest stellar populations (~few Myr). On the other hand, the total infrared luminosity (the one of the two parameters that shape IR8) traces emission by dust heated by stellar population up to ~100 Myr. As a consequence, changes in the line ratios can occur on much shorter timescales than changes in IR8, if the starburst has been occurring for more than 10 Myr. That could also offer an alternative explanation for the variation of IR8 as a function of $EW_{6.2}$; IR8 variations could result from a mechanism that affects L_{IR}, but not the PAH emission, such as a contribution of an old stellar population to L_{IR}. That would suggest that galaxies with higher IR8 values are galaxies that have experienced an older starburst event and their bolometric infrared output, L_{IR}, significant contributes by dust heated by old stellar populations. However, as shown by Elbaz et al. (2011), high IR8 values in the local Universe, but also at high-z, are predominantly found among galaxies that are experiencing a recent star-burst event with high specific star formation rates (such as local ULIRGs and SMGs). In the above framework, a harder radiation field would also result in a larger number of UV photons per dust particle, or equally in a higher dust-mass-weighted luminosity, L_{IR}/M_{dust}. Indeed, this quantity reflects the amount of available energy per dust mass unit, under the assumption that the majority of the UV photons are eventually absorbed by dust and are re-emitted in the IR. We note that in the DL07 models the dust-mass-weighted luminosity is proportional to the mean radiation field ($\langle U \rangle$) and is a good proxy of the dust temperature of the ISM of the galaxy (Magdis et al. 2012b). As shown in Fig. 10 (right), L_{IR}/M_{dust} correlates with [Ne III]/[Ne II], albeit with a considerable scatter, suggesting that the dust-mass-weighted luminosity (or T_d) traces the hardness of the radiation field in star-forming galaxies.

Differential line extinction due to gas density variations can also cause a decrease in the observed [Ne III]/[Ne II] ratio. For example, Farrah et al. (2007) argued for an increased density of gas in local ULIRGs based on their lower [Ne III]/[Ne II] ratios (for a given [S IV]/[S III]) compared with those of systems with lower infrared luminosities. However, a sole increase in gas density cannot explain the observed L_{IR}/M_{dust} − [Ne III]/[Ne II] correlation in our sample. Finally, metallicity effects could also play a role. Galaxies with lower IR8 or PAH emission could simply be more metal-rich and therefore have more PAHs, resulting in higher L_8 for a given L_{IR}. While [Ne III]/[Ne II] is not expected to be directly affected by metallicity variations, various studies have shown that the [Ne III]/[Ne II] ratios in low-metallicity galaxies are very high (>3), often one to two orders of magnitude greater than in more metal-rich starburst galaxies (e.g., Rigby & Rieke 2004; Madden et al. 2006; Wu et al. 2006). Metal poor

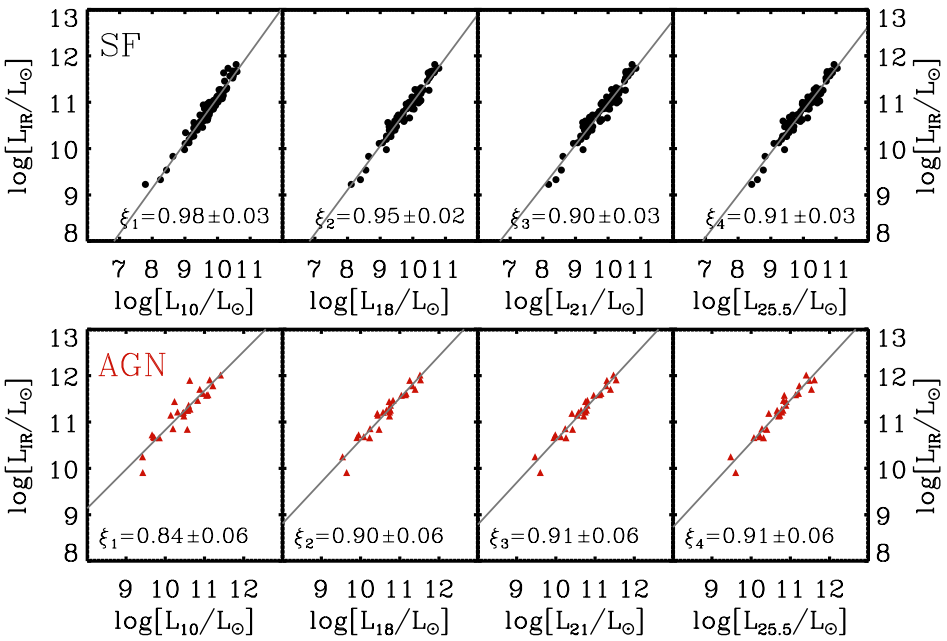


Fig. 11. Correlation between $L_{\rm IR}$ and rest-frame luminosities at observed 10, 18, 21-, and 25.5 μm. The choice of the rest-frame luminosity wavelengths corresponds to the central wavelengths of the JWST-MIRI filters. Each IRS spectrum was shifted to the rest-frame and convolved with MIRI filters. The best-fit regression line and the associated plot are shown in each panel and are summarised in Table 3.

Table 3. Scaling relations between $L_{\rm IR}$ and various MIRI broad-band luminosities.

y/x	$\log(L_{10}/L_\odot)$	$\log(L_{18}/L_\odot)$	$\log(L_{21}/L_\odot)$	$\log(L_{25.5}/L_\odot)$
$\log(L_{\rm IR}/L_\odot)$ (SF)	$\alpha = 1.33 \pm 0.32, \beta = 0.98 \pm 0.03$	$1.52 \pm 0.22, 0.95 \pm 0.02$	$1.98 \pm 0.27, 0.90 \pm 0.03$	$1.69 \pm 0.28, 0.91 \pm 0.03$
$\log(L_{\rm IR}/L_\odot)$ (AGN)	$\alpha = 2.34 \pm 0.72, \beta = 0.84 \pm 0.06$	$1.55 \pm 0.65, 0.90 \pm 0.06$	$1.46 \pm 0.64, 0.91 \pm 0.06$	$1.39 \pm 0.69, 0.91 \pm 0.06$

Notes. $y = \alpha + \beta \times x$, where $y = \log L_{\rm IR}$ and x the corresponding MIRI luminosities.

galaxies also tend to exhibit lower (by a factor of 10) $L^{\rm PAH}_{\rm TOT}/L_{15}$ ratios than metal-rich starbursts (Madden et al. 2006). While not conclusive, the fact that our sample exhibits only a narrow range in the [Ne III]/[Ne II] ($0.1 < $ [Ne III]/[Ne II] < 0.8) and $L^{\rm TOT}_{\rm PAH}$ values, and does not extend to values similar to those of local metal poor dwarfs suggests that metallicity is not the main driver of the observed dispersion.

While a firm conclusion cannot be reached, it appears that the PAH deficit with respect to $L_{\rm IR}$ in star-forming galaxies with higher IR8 values is caused by PAH destruction due to harder radiation fields that also result in higher dust temperatures. These characteristics could be indicative of a more compact star-formation geometry, which is in line with the recently proposed correlation between IR8, compactness of the projected star-formation density, and excess in the specific star formation rate (e.g., Diaz Santos et al. 2011; Elbaz et al. 2011). However, a proper study of the spatial extent of the PAH emission and of the star-forming regions in distant galaxies as traced by the mid-IR emission will have to wait for the launch of the *James Webb* Space Telescope (JWST). Given that a large number of distant galaxies that will be detected with MIRI onboard JWST will lack detection in longer wavelengths it will be extremely useful to have scaling relations between the mid-IR and total infrared luminosity. Using the observed IRS spectra of the galaxies and the total infrared luminosity as inferred from the addition of the *Herschel* data, we provide total luminosity calibrations based on monochromatic luminosities at 10-, 18-, 21- and 25.5-μm as they will be traced by MIRI for AGN-dominated and star-forming galaxies (Fig. 11 and Table 3).

6. Conclusions

We have used a 24 μm-selected flux-limited sample of 154 $z \sim 0.15$ galaxies all chosen to benefit from ancillary IRS spectra and new *Herschel* SPIRE photometry as part of the HerMES programme to construct their full IR SEDs. Based on SED decomposition, on the relative strength of the 6.2 μm PAH feature with respect to the mid-IR continuum, and on the IRAC colours of the sources, we have identified the dominant mechanism that powers their infrared emission, classified them as AGN and star-forming-dominated galaxies and investigated in detail their mid-to-far-IR properties. Our main findings are summarised as follows:

- We found a statistically insignificant effect of the presence of an AGN on the temperature of the cold dust of the host galaxy. AGN-dominated sources exhibit a marginally higher cold dust temperature, suggesting that the far-IR colours are mainly shaped by star formation activity.
- Star-forming galaxies show an anti-correlation between the IR8 = $L_{\rm IR}/L_8$ and the 6.2 μm PAH feature $EW_{6.2}$. Our analysis suggests that for galaxies with $EW_{6.2} \geq 0.4$ μm (i.e. star-forming galaxies), differences in the $EW_{6.2}$, for fixed $L_{\rm IR}$, are driven by variations in the PAH emission and not by a varying 5–15 μm underlying continuum.
- For star-formation-dominated sources we confirm that the strength of the PAH emission anti-correlates with the hardness of the radiation field as traced by the [Ne III]/[Ne II] ratio.
- The dust-mass-weighted luminosity $L_{\rm IR}/M_{\rm dust}$, correlates with the [Ne III]/[Ne II] ratio, suggesting that sources with harder interstellar radiation fields are characterised by higher dust temperatures.

Overall, it appears that the decrease in the PAH strength, for fixed $L_{\rm IR}$, is caused by harder radiation fields that are characterised by high dust-mass-weighted luminosities and dust temperatures. While this is in line with recent evidence that link the

IR8 with the compactness of the star-forming regions, the upcoming JWST mission will allow for a more detailed investigation both in local and in distant galaxies.

Acknowledgements. GEM acknowledges support from the John Fell Oxford University Press (OUP) Research Fund and the University of Oxford. A.A.-H. acknowledges funding through the Universidad de Cantabria August G. Linares Programme. VC acknowledges partial support from the EU FP7 Grant PIRSES-GA-20120316788. This paper uses data from *Herschel*'s photometer SPIRE. SPIRE has been developed by a consortium of institutes led by Cardiff University (UK) and including Univ. Lethbridge (Canada); NAOC (China); CEA, LAM (France); IFSI, Univ. Padua (Italy); IAC (Spain); Stockholm Observatory (Sweden); Imperial College London, RAL, UCL-MSSL, UKATC, Univ. Sussex (UK); and Caltech, JPL, NHSC, Univ. Colorado (USA).

References

Abel, N. P., Dudley, C., Fischer, J., Satyapal, S., & van Hoof, P. A. M. 2009, ApJ, 701, 1147
Allamandola, L. J., Tielens, A. G. G. M., & Barker, J. R. 1989, ApJS, 71, 733
Alonso-Herrero, A., Pérez-González, P. G., Alexander, D. M., et al. 2006, ApJ, 640, 167
Armus, L., Charmandaris, V., Bernard-Salas, J., et al. 2007, ApJ, 656, 148
Berta, S., Magnelli, B., Nordon, R., et al. 2011, A&A, 532, A49
Brandl, B. R., Bernard-Salas, J., Spoon, H. W. W., et al. 2006, ApJ, 653, 1129
Carral, P., Hollenbach, D. J., Lord, S. D., et al. 1994, ApJ, 423, 223
Dale, D. A., & Helou, G. 2002, ApJ, 576, 159
Dale, D. A., Aniano, G., Engelbracht, C. W., et al. 2012, ApJ, 745, 95
Dasyra, K. M., Yan, L., Helou, G., et al. 2009, ApJ, 701, 1123
Desai, V., Armus, L., Spoon, H. W. W., et al. 2007, ApJ, 669, 810
Desai, V., Soifer, B. T., Dey, A., et al. 2009, ApJ, 700, 1190
Díaz-Santos, T., Charmandaris, V., Armus, L., et al. 2010, ApJ, 723, 993
Díaz-Santos, T., Charmandaris, V., Armus, L., et al. 2011, ApJ, 741, 32
Dole, H., Lagache, G., Puget, J.-L., et al. 2006, A&A, 451, 417
Donley, J. L., Rieke, G. H., Pérez-González, P. G., Rigby, J. R., & Alonso-Herrero, A. 2007, ApJ, 660, 167
Donley, J. L., Koekemoer, A. M., Brusa, M., et al. 2012, ApJ, 748, 142
Draine, B. T., & Li, A. 2007, ApJ, 657, 810
Draine, B. T., Dale, D. A., Bendo, G., et al. 2007, ApJ, 663, 866
Dunne, L., & Eales, S. A. 2001, MNRAS, 327, 697
Dunne, L., Eales, S., Edmunds, M., et al. 2000, MNRAS, 315, 115
Dupac, X., Giard, M., Bernard, J.-P., et al. 2001, ApJ, 553, 604
Elbaz, D., Hwang, H. S., Magnelli, B., et al. 2010, A&A, 518, L29
Elbaz, D., Dickinson, M., Hwang, H. S., et al. 2011, A&A, 533, A119
Fadda, D., Marleau, F. R., Storrie-Lombardi, L. J., et al. 2006, AJ, 131, 2859
Farrah, D., Bernard-Salas, J., Spoon, H. W. W., et al. 2007, ApJ, 667, 149
Farrah, D., Lonsdale, C. J., Weedman, D. W., et al. 2008, ApJ, 677, 957
Feltre, A., Hatziminaoglou, E., Hernán-Caballero, A., et al. 2013, MNRAS, 434, 2426
Galliano, F., Madden, S. C., Tielens, A. G. G. M., Peeters, E., & Jones, A. P. 2008, ApJ, 679, 310
Graciá-Carpio, J., Sturm, E., Hailey-Dunsheath, S., et al. 2011, ApJ, 728, L7
Genzel, R., & Cesarsky, C. J. 2000, ARA&A, 38, 761
Genzel, R., Lutz, D., Sturm, E., et al. 1998, ApJ, 498, 579
Gordon, K. D., Galliano, F., Hony, S., et al. 2010, A&A, 518, L89
Griffin, M. J., Abergel, A., Abreu, A., et al. 2010, A&A, 518, L3
Haas, M., Klaas, U., Müller, S. A. H., et al. 2003, A&A, 402, 87
Hatziminaoglou, E., Omont, A., Stevens, J. A., et al. 2010, A&A, 518, L33
Hernán-Caballero, A., Pérez-Fournon, I., Hatziminaoglou, E., et al. 2009, MNRAS, 395, 1695
Hildebrand, R. H. 1983, QJRAS, 24, 267
Houck, J. R., Roellig, T. L., van Cleve, J., et al. 2004, ApJS, 154, 18
Huang, J.-S., Faber, S. M., Daddi, E., et al. 2009, ApJ, 700, 183
Imanishi, M., Dudley, C. C., Maiolino, R., et al. 2007, ApJS, 171, 72
Kennicutt, R. C., Jr. 1998, ARA&A, 36, 189
Kessler, M. F., Steinz, J. A., Anderegg, M. E., et al. 1996, A&A, 315, L27
Kirkpatrick, A., Pope, A., Alexander, D. M., et al. 2012, ApJ, 759, 139
Kirkpatrick, J. D., Gelino, C. R., Cushing, M. C., et al. 2012, ApJ, 753, 156
Lacy, M., Storrie-Lombardi, L. J., Sajina, A., et al. 2004, ApJS, 154, 166
Lagache, G., Puget, J.-L., & Dole, H. 2005, ARA&A, 43, 727
Laurent, O., Mirabel, I. F., Charmandaris, V., et al. 2000, A&A, 359, 887
Le Floc'h, E., Papovich, C., Dole, H., et al. 2005, ApJ, 632, 169
Li, A., & Draine, B. T. 2001, ApJ, 554, 778
Li, A., & Draine, B. T. 2002, ApJ, 572, 232
Lonsdale, C. J., Lonsdale, C. J., Smith, H. E., & Diamond, P. J. 2003, ApJ, 592, 804
Lutz, D., Genzel, R., Sternberg, A., et al. 1996, A&A, 315, L137
Lutz, D., Sturm, E., Tacconi, L. J., et al. 2008, ApJ, 684, 853
Madden, S. C., Galliano, F., Jones, A. P., & Sauvage, M. 2006, A&A, 446, 877
Magdis, G. E., Elbaz, D., Dickinson, M., et al. 2011, A&A, 534, A15
Magdis, G. E., Daddi, E., Béthermin, M., et al. 2012, ApJ, 760, 6
Mendez, A. J., Coil, A. L., Aird, J., et al. 2013, ApJ, 770, 40
Menéndez-Delmestre, K., Blain, A. W., Smail, I., et al. 2009, ApJ, 699, 667
Mullaney, J. R., Alexander, D. M., Goulding, A. D., & Hickox, R. C. 2011, MNRAS, 414, 1082
Mullaney, J. R., Pannella, M., Daddi, E., et al. 2012, MNRAS, 419, 95
Netzer, H., Lutz, D., Schweitzer, M., et al. 2007, ApJ, 666, 806
Nguyen, H. T., Schulz, B., Levenson, L., et al. 2010, A&A, 518, L5
Oliver, S. J., Wang, L., Smith, A. J., et al. 2010, A&A, 518, L21
Oliver, S. J., Bock, J., Altieri, B., et al. 2012, MNRAS, 424, 1614
Park, S. Q., Barmby, P., Willner, S. P., et al. 2010, ApJ, 717, 1181
Peeters, E., Martín-Hernández, N. L., Damour, F., et al. 2002, A&A, 381, 571
Peeters, E., Spoon, H. W. W., & Tielens, A. G. G. M. 2004, ApJ, 613, 986
Pereira-Santaella, M., Alonso-Herrero, A., Rieke, G. H., et al. 2010, ApJS, 188, 447
Pilbratt, G. L., Riedinger, J. R., Passvogel, T., et al. 2010, A&A, 518, L1
Pope, A., Chary, R.-R., Alexander, D. M., et al. 2008, ApJ, 675, 1171
Puget, J. L., Leger, A., & Boulanger, F. 1985, A&A, 142, L19
Puget, J.-L., Abergel, A., Bernard, J.-P., et al. 1996, A&A, 308, L5
Rigby, J. R., & Rieke, G. H. 2004, ApJ, 606, 237
Rigopoulou, D., Spoon, H. W. W., Genzel, R., et al. 1999, AJ, 118, 2625
Rodighiero, G., Cimatti, A., Gruppioni, C., et al. 2010, A&A, 518, L25
Roseboom, I. G., Oliver, S. J., Kunz, M., et al. 2010, MNRAS, 409, 48
Roseboom, I. G., Ivison, R. J., Greve, T. R., et al. 2012, MNRAS, 419, 2758
Sajina, A., Yan, L., Armus, L., et al. 2007, ApJ, 664, 713
Sargsyan, L., Weedman, D., Lebouteiller, V., et al. 2011, ApJ, 730, 19
Siebenmorgen, R., Krügel, E., & Spoon, H. W. W. 2004, A&A, 414, 123
Smith, J. D. T., Draine, B. T., Dale, D. A., et al. 2007, ApJ, 656, 770
Soifer, B. T., & Neugebauer, G. 1991, AJ, 101, 354
Soifer, B. T., Neugebauer, G., Matthews, K., Egami, E., & Weinberger, A. J. 2002, AJ, 124, 2980
Spoon, H. W. W., Marshall, J. A., Houck, J. R., et al. 2007, ApJ, 654, L49
Stern, D., Eisenhardt, P., Gorjian, V., et al. 2005, ApJ, 631, 163
Thornley, M. D., Schreiber, N. M. F., Lutz, D., et al. 2000, ApJ, 539, 641
Uchida, K. I., Sellgren, K., & Werner, M. 1998, ApJ, 493, L109
Weedman, D. W., Hao, L., Higdon, S. J. U., et al. 2005, ApJ, 633, 706
Weedman, D., Polletta, M., Lonsdale, C. J., et al. 2006, ApJ, 653, 101
Weingartner, J. C., & Draine, B. T. 2001, ApJ, 548, 296
Werner, M. W., Roellig, T. L., Low, F. J., et al. 2004, ApJS, 154, 1
Wu, Y., Charmandaris, V., Hao, L., et al. 2006, ApJ, 639, 157
Wu, Y., Helou, G., Armus, L., et al. 2010, ApJ, 723, 895
Yan, L., Sajina, A., Fadda, D., et al. 2007, ApJ, 658, 778

Pages 15 to 20 are available in the electronic edition of the journal at http://www.aanda.org

Table 1. *Herschel* SPIRE photometry of the 5MUSES sample.

Name	$z_{\rm spec}$	S_{24} [mJy]	S_{250} [mJy]	S_{350} [mJy]	S_{500} [mJy]
J021503.52-042421.6	0.137	5.2 ± 0.3	19.4 ± 2.4	–	–
J021557.11-033729.0	0.032	8.8 ± 0.4	123.5 ± 2.4	58.2 ± 2.6	21.0 ± 3.4
J021649.71-042554.8	0.143	10.1 ± 0.5	33.5 ± 2.5	–	–
J021743.82-051751.7	0.031	17.1 ± 0.9	190.9 ± 2.4	89.9 ± 2.6	44.9 ± 3.0
J021754.88-035826.4	0.226	10.3 ± 0.5	138.2 ± 2.3	83.2 ± 2.5	41.1 ± 3.1
J021849.76-052158.2	0.292	5.3 ± 0.3	61.7 ± 2.4	20.7 ± 2.5	–
J021859.74-040237.2	0.199	15.9 ± 0.8	34.5 ± 2.4	19.0 ± 2.4	–
J021916.05-055726.9	0.103	11.0 ± 0.6	45.7 ± 2.8	25.3 ± 3.0	20.2 ± 3.4
J021928.33-042239.8	0.042	17.3 ± 0.9	43.9 ± 2.5	21.7 ± 2.4	–
J021939.08-051133.8	0.151	32.5 ± 1.6	60.6 ± 2.1	25.8 ± 2.2	–
J021953.04-051824.1	0.072	30.3 ± 1.5	157.6 ± 2.2	72.9 ± 2.2	27.8 ± 2.8
J021956.96-052440.4	0.081	5.6 ± 0.3	70.8 ± 2.5	38.0 ± 2.3	–
J022005.93-031545.7	1.560	6.9 ± 0.3	37.5 ± 2.4	38.5 ± 4.7	–
J022145.09-053207.4	0.008	6.2 ± 0.3	36.5 ± 2.1	22.0 ± 2.2	–
J022147.82-025730.7	0.068	21.0 ± 1.1	218.2 ± 2.4	96.0 ± 2.9	27.0 ± 4.4
J022147.87-044613.5	0.025	5.1 ± 0.3	20.3 ± 2.5	–	–
J022151.54-032911.8	0.164	6.9 ± 0.3	51.1 ± 2.5	27.6 ± 2.8	–
J022205.03-050537.0	0.258	6.3 ± 0.3	96.5 ± 2.4	47.1 ± 2.7	22.5 ± 4.7
J022223.26-044319.8	0.073	5.1 ± 0.3	40.3 ± 2.4	–	–
J022224.06-050550.3	0.149	5.7 ± 0.3	33.5 ± 2.5	–	30.8 ± 2.8
J022241.34-045652.0	0.139	5.1 ± 0.3	30.6 ± 2.4	–	–
J022257.96-041840.8	0.239	5.3 ± 0.3	48.5 ± 2.3	23.6 ± 2.5	–
J022301.97-052335.8	0.708	6.8 ± 0.3	141.8 ± 2.4	73.3 ± 2.4	39.1 ± 3.1
J022315.58-040606.0	0.199	9.4 ± 0.5	76.3 ± 2.1	38.4 ± 2.5	24.4 ± 2.6
J022329.13-043209.5	0.144	7.6 ± 0.4	50.0 ± 2.5	–	–
J022334.65-035229.4	0.176	7.6 ± 0.4	25.8 ± 2.3	–	–
J022345.04-054234.4	0.143	9.1 ± 0.5	58.7 ± 2.3	22.7 ± 2.2	–
J022413.64-042227.8	0.116	9.2 ± 0.5	55.3 ± 2.3	25.8 ± 2.6	–
J022422.48-040230.5	0.171	7.5 ± 0.4	31.4 ± 2.4	–	–
J022431.58-052818.8	2.068	9.4 ± 0.5	45.7 ± 2.4	42.0 ± 2.3	28.1 ± 3.5
J022434.28-041531.2	0.259	6.3 ± 0.3	73.1 ± 2.4	21.8 ± 3.5	–
J022438.97-042706.3	0.252	6.6 ± 0.3	31.4 ± 2.4	27.8 ± 2.4	24.6 ± 3.0
J022446.99-040851.3	0.096	5.3 ± 0.3	131.8 ± 2.4	41.5 ± 3.9	–
J022457.64-041417.9	0.063	11.9 ± 0.6	166.6 ± 2.3	91.5 ± 2.5	33.3 ± 6.1
J022507.43-041835.7	0.105	6.8 ± 0.3	66.1 ± 2.2	31.4 ± 2.3	20.4 ± 2.6
J022522.59-045452.2	0.144	10.1 ± 0.5	115.1 ± 2.4	53.1 ± 3.7	–
J022536.44-050011.5	0.053	13.7 ± 0.7	474.6 ± 2.5	205.1 ± 2.6	75.1 ± 3.6
J022548.21-050051.5	0.150	8.0 ± 0.4	59.1 ± 2.3	–	–
J022549.78-040024.6	0.044	58.5 ± 2.9	186.1 ± 2.5	73.5 ± 2.7	30.0 ± 3.2
J022559.99-050145.3	0.205	5.7 ± 0.3	68.4 ± 2.6	30.3 ± 2.3	–
J022602.92-045306.8	0.056	6.4 ± 0.3	59.3 ± 2.4	31.4 ± 2.5	24.8 ± 2.7
J022603.61-045903.8	0.055	31.4 ± 1.6	167.6 ± 2.5	75.7 ± 2.4	30.2 ± 3.1
J022617.43-050443.4	0.057	48.7 ± 2.4	79.9 ± 2.5	35.5 ± 2.5	–
J022637.79-035841.6	0.070	13.5 ± 0.7	28.4 ± 2.5	18.4 ± 4.0	–
J022655.87-040302.2	0.135	6.9 ± 0.3	16.1 ± 2.4	–	–
J022720.68-044537.1	0.055	73.1 ± 3.7	329.5 ± 2.5	140.4 ± 2.4	52.0 ± 3.5
J022738.53-044702.7	0.173	7.1 ± 0.4	25.6 ± 2.4	–	–
J022741.64-045650.5	0.055	11.4 ± 0.6	126.1 ± 2.5	56.6 ± 2.6	31.8 ± 3.0
J103237.44+580845.9	0.251	6.1 ± 0.3	169.7 ± 8.0	62.3 ± 3.5	–
J103450.50+584418.2	0.091	20.1 ± 1.0	99.0 ± 6.4	44.2 ± 9.5	–
J103513.72+573444.6	1.537	5.5 ± 0.3	69.5 ± 4.3	45.3 ± 3.6	33.0 ± 5.4
J103527.20+583711.9	0.885	6.9 ± 0.3	52.8 ± 4.1	42.5 ± 4.1	21.3 ± 6.6
J103531.46+581234.2	0.176	5.0 ± 0.3	108.6 ± 5.1	43.5 ± 4.8	–
J103542.76+583313.1	0.087	6.6 ± 0.3	27.7 ± 4.4	–	–
J103601.81+581836.2	0.100	6.0 ± 0.3	53.3 ± 3.9	21.3 ± 4.5	–
J103646.42+584330.6	0.140	6.8 ± 0.3	60.2 ± 3.9	18.0 ± 4.2	–
J103803.35+572701.5	1.285	15.4 ± 0.8	70.5 ± 4.3	37.8 ± 4.3	–
J103813.90+580047.3	0.205	6.2 ± 0.3	30.8 ± 4.4	17.0 ± 4.4	–
J103856.16+570333.9	0.178	5.7 ± 0.3	16.6 ± 4.3	–	–
J104016.32+570846.0	0.118	5.2 ± 0.3	63.6 ± 5.6	–	–
J104058.79+581703.3	0.072	10.4 ± 0.5	16.8 ± 4.1	–	–
J104131.79+592258.4	0.925	7.0 ± 0.4	41.0 ± 4.3	–	–
J104132.49+565953.0	0.346	8.3 ± 0.4	21.0 ± 4.0	–	–
J104159.83+585856.4	0.360	21.7 ± 1.1	31.5 ± 4.9	17.7 ± 5.3	–
J104255.66+575549.7	1.468	6.4 ± 0.3	23.3 ± 4.1	–	–

Table 1. continued.

Name	z_{spec}	S_{24} [mJy]	S_{250} [mJy]	S_{350} [mJy]	S_{500} [mJy]
J104432.94+564041.6	0.067	28.7 ± 1.4	286.5 ± 5.1	114.4 ± 4.4	31.8 ± 6.9
J104438.21+562210.7	0.025	80.6 ± 4.0	590.6 ± 7.4	231.0 ± 5.3	84.6 ± 5.6
J104454.08+574425.7	0.118	6.5 ± 0.3	165.3 ± 4.9	77.3 ± 4.7	–
J104516.02+592304.7	0.322	5.1 ± 0.3	19.4 ± 4.1	–	–
J104643.26+584715.1	0.140	5.4 ± 0.3	102.4 ± 4.5	42.1 ± 5.6	–
J104705.07+590728.4	0.391	7.0 ± 0.4	16.1 ± 4.3	–	–
J104729.89+572842.9	0.230	6.2 ± 0.3	136.0 ± 4.8	72.8 ± 4.5	26.6 ± 7.5
J104837.81+582642.1	0.232	7.6 ± 0.4	114.0 ± 4.3	46.5 ± 4.8	–
J104843.90+580341.2	0.162	7.1 ± 0.4	36.8 ± 6.5	–	–
J104907.15+565715.3	0.072	9.7 ± 0.5	106.9 ± 4.1	31.8 ± 4.4	–
J105005.97+561500.0	0.119	14.8 ± 0.7	106.9 ± 3.7	44.0 ± 3.8	27.9 ± 7.4
J105047.83+590348.3	0.131	5.2 ± 0.3	75.1 ± 5.4	32.4 ± 4.1	–
J105106.12+591625.3	0.768	5.4 ± 0.3	29.8 ± 6.5	–	–
J105128.05+573502.4	0.073	10.0 ± 0.5	54.6 ± 4.4	24.4 ± 4.4	–
J105158.53+590652.0	1.814	5.4 ± 0.3	48.7 ± 5.2	40.7 ± 8.4	–
J105200.29+591933.7	0.115	11.4 ± 0.6	31.3 ± 5.1	–	–
J105206.56+580947.1	0.117	16.7 ± 0.8	247.5 ± 6.0	97.7 ± 5.8	–
J105336.87+580350.7	0.460	5.9 ± 0.3	33.3 ± 4.7	–	–
J105404.11+574019.7	1.101	8.5 ± 0.4	15.5 ± 4.2	–	–
J105421.65+582344.6	0.205	16.8 ± 0.8	114.7 ± 4.1	39.9 ± 3.8	–
J105604.84+574229.9	1.211	11.2 ± 0.6	36.6 ± 6.9	28.5 ± 8.7	–
J105636.95+573449.3	0.047	6.4 ± 0.3	109.9 ± 4.5	35.6 ± 5.6	–
J105641.81+580046.0	0.130	7.5 ± 0.4	104.9 ± 4.2	34.1 ± 4.0	–
J105705.43+580437.4	0.140	16.5 ± 0.8	129.1 ± 4.6	47.4 ± 4.7	–
J105733.53+565737.4	0.086	5.6 ± 0.3	26.1 ± 5.3	–	–
J105740.55+570616.4	0.073	6.1 ± 0.3	34.7 ± 3.9	–	–
J105903.47+572155.1	0.119	13.8 ± 0.7	60.9 ± 4.5	–	–
J105951.71+581802.9	2.335	5.3 ± 0.3	29.7 ± 4.6	41.8 ± 4.8	27.0 ± 8.8
J105959.95+574848.1	0.453	9.1 ± 0.5	37.8 ± 5.2	–	–
J110002.06+573142.1	0.387	8.3 ± 0.4	64.0 ± 4.3	–	–
J110124.97+574315.8	0.243	6.1 ± 0.3	47.1 ± 4.1	25.2 ± 4.7	–
J110133.80+575206.6	0.277	6.4 ± 0.3	136.3 ± 5.2	58.2 ± 4.5	30.6 ± 6.5
J110223.58+574436.2	0.226	10.2 ± 0.5	27.0 ± 5.1	17.4 ± 5.5	–
J110235.02+574655.7	0.226	6.2 ± 0.3	44.2 ± 4.3	–	–
J160408.18+542531.2	0.260	5.0 ± 0.3	62.4 ± 1.5	33.1 ± 1.6	–
J160655.35+534016.9	0.214	14.6 ± 0.7	30.1 ± 1.6	23.1 ± 1.5	–
J160803.71+545301.9	0.053	5.1 ± 0.3	180.7 ± 1.5	76.2 ± 1.6	25.8 ± 2.6
J160832.59+552926.9	0.065	5.9 ± 0.3	102.9 ± 1.8	50.6 ± 1.6	–
J160858.38+553010.2	0.066	8.8 ± 0.4	101.7 ± 1.3	37.2 ± 1.2	–
J160907.56+552428.4	0.065	7.7 ± 0.4	128.1 ± 1.5	57.9 ± 1.5	19.1 ± 2.0
J160908.28+552241.4	0.084	6.6 ± 0.3	110.9 ± 1.5	42.5 ± 1.7	–
J160926.69+551642.3	0.068	6.8 ± 0.3	81.7 ± 1.5	35.8 ± 1.9	–
J160931.55+541827.3	0.082	5.6 ± 0.3	105.1 ± 1.5	35.0 ± 1.5	–
J160937.48+541259.2	0.086	5.7 ± 0.3	129.7 ± 1.5	58.0 ± 1.5	22.1 ± 2.0
J161103.73+544322.0	0.063	6.6 ± 0.3	71.4 ± 1.5	29.4 ± 3.3	–
J161123.44+545158.2	0.078	5.5 ± 0.3	56.2 ± 1.6	21.4 ± 1.5	–
J161223.39+540339.2	0.138	13.0 ± 0.6	70.5 ± 1.6	28.1 ± 1.9	–
J161233.43+545630.4	0.083	8.3 ± 0.4	185.3 ± 1.5	87.0 ± 1.8	38.3 ± 3.5
J161241.05+543956.8	0.035	5.7 ± 0.3	22.0 ± 1.5	–	–
J161250.85+532304.9	0.048	17.9 ± 0.9	114.6 ± 1.6	46.3 ± 1.2	18.6 ± 1.9
J161254.17+545525.4	0.065	8.0 ± 0.4	257.0 ± 1.6	123.6 ± 1.5	49.4 ± 1.8
J161357.01+534105.3	0.180	6.5 ± 0.3	45.9 ± 1.6	32.9 ± 1.8	22.9 ± 2.1
J161411.52+540554.3	0.305	5.9 ± 0.3	47.7 ± 1.6	28.5 ± 1.8	19.2 ± 1.9
J161521.78+543148.3	0.474	5.1 ± 0.3	21.7 ± 1.5	–	–
J161551.45+541535.9	0.215	6.3 ± 0.3	98.7 ± 1.5	42.0 ± 1.5	–
J161645.92+542554.4	0.223	12.4 ± 0.6	31.4 ± 1.6	–	–
J161759.22+541501.3	0.135	22.7 ± 1.1	35.8 ± 2.4	16.5 ± 3.1	–
J161819.31+541859.0	0.083	28.3 ± 1.4	378.9 ± 1.7	153.5 ± 1.9	51.4 ± 3.1
J171033.21+584456.8	0.281	6.1 ± 0.3	43.7 ± 2.8	–	–
J171232.34+592125.9	0.210	8.7 ± 0.4	138.9 ± 3.0	85.3 ± 3.2	36.9 ± 4.2
J171233.38+583610.5	1.663	5.1 ± 0.3	20.7 ± 2.5	–	–
J171233.77+594026.4	0.217	5.1 ± 0.3	36.4 ± 3.4	–	–
J171316.50+583234.9	0.079	6.7 ± 0.3	139.5 ± 3.1	60.7 ± 3.0	21.5 ± 3.6
J171414.81+585221.5	0.167	9.0 ± 0.5	38.5 ± 2.5	–	–
J171419.98+602724.6	2.990	5.6 ± 0.3	17.9 ± 2.5	–	–
J171446.47+593400.1	0.129	7.5 ± 0.4	96.9 ± 2.8	34.3 ± 3.1	–

Table 1. continued.

Name	z_{spec}	S_{24} [mJy]	S_{250} [mJy]	S_{350} [mJy]	S_{500} [mJy]
J171447.31+583805.9	0.257	5.4 ± 0.3	61.3 ± 2.7	27.5 ± 2.3	–
J171513.88+594638.1	0.248	5.1 ± 0.3	60.6 ± 2.6	25.1 ± 2.8	–
J171550.50+593548.8	0.066	9.1 ± 0.5	123.7 ± 2.8	63.2 ± 2.7	25.5 ± 3.6
J171614.48+595423.8	0.153	8.6 ± 0.4	107.5 ± 2.9	45.6 ± 2.8	–
J171630.23+601422.7	0.107	8.6 ± 0.4	41.7 ± 2.5	–	–
J171650.58+595751.4	0.182	6.8 ± 0.3	17.0 ± 3.2	–	–
J171711.11+602710.0	0.110	9.5 ± 0.5	58.7 ± 2.4	20.0 ± 2.6	–
J171747.51+593258.1	0.248	5.3 ± 0.3	22.3 ± 2.4	–	–
J171852.71+591432.0	0.322	14.0 ± 0.7	51.4 ± 2.6	24.7 ± 2.8	–
J171933.37+592742.8	0.139	7.6 ± 0.4	128.3 ± 2.8	45.4 ± 2.7	–
J171944.91+595707.7	0.069	14.4 ± 0.7	135.3 ± 3.2	50.4 ± 3.1	–
J172043.28+584026.6	0.125	9.7 ± 0.5	144.8 ± 2.8	50.8 ± 2.6	–
J172044.86+582924.0	1.697	5.3 ± 0.3	24.1 ± 2.7	–	–
J172159.43+595034.3	0.028	9.7 ± 0.5	146.5 ± 2.7	62.2 ± 2.9	–
J172219.58+594506.9	0.272	7.8 ± 0.4	25.2 ± 3.2	19.0 ± 3.3	–
J172228.04+601526.0	0.742	7.2 ± 0.4	40.1 ± 3.0	18.3 ± 3.8	–
J172238.73+585107.0	1.624	6.7 ± 0.3	54.1 ± 2.5	42.8 ± 2.9	29.0 ± 3.4
J172313.06+590533.1	0.108	6.2 ± 0.3	61.1 ± 2.4	24.4 ± 2.8	–
J172355.58+601301.7	0.175	5.4 ± 0.3	89.4 ± 2.6	36.8 ± 2.7	19.3 ± 3.4
J172355.97+594047.6	0.030	5.2 ± 0.3	27.2 ± 2.4	–	–
J172402.11+600601.4	0.156	8.0 ± 0.4	70.7 ± 5.0	–	–
J172546.80+593655.3	0.035	26.0 ± 1.3	461.0 ± 4.5	201.7 ± 2.9	83.6 ± 3.9
J172551.35+601138.9	0.029	27.3 ± 1.4	266.7 ± 3.4	115.8 ± 3.0	44.0 ± 2.9

Table 2. Physical Properties of the 5MUSES sample as derived based on the DL07 and MBB models.

Name	z_{spec}	$\log L_{IR}$ $[L_\odot]$	$\log M_{dust}$[a] $[M_\odot]$	γ –	U_{min} –	T_d[b] [K]	AGN[c] frac.
J021503.52-042421.6	0.137	10.86 ± 0.04	8.01 ± 0.07	1.0	5	–	0.06
J021557.11-033729.0	0.032	9.83 ± 0.02	7.18 ± 0.09	1.5	3	26 ± 1	0.00
J021638.21-042250.8	0.143	10.99 ± 0.01	–	–	–	–	0.58
J021640.72-044405.1	0.031	10.11 ± 0.01	7.29 ± 0.07	0.7	5	28 ± 1	0.08
J021649.71-042554.8	0.226	11.67 ± 0.01	8.76 ± 0.03	3.0	5	31 ± 2	0.36
J021657.77-032459.7	0.292	11.64 ± 0.03	8.35 ± 0.02	0.7	12	35 ± 1	0.16
J021729.06-041937.8	0.199	11.13 ± 0.01	–	–	–	–	0.12
J021743.01-043625.1	0.103	10.66 ± 0.01	–	–	–	30 ± 1	0.74
J021743.82-051751.7	0.042	9.98 ± 0.01	6.50 ± 0.06	10.0	10	35 ± 7	0.29
J021754.88-035826.4	0.151	11.36 ± 0.01	–	–	–	36 ± 1	0.58
J021808.22-045845.3	0.072	10.86 ± 0.04	7.75 ± 0.03	3.0	8	32 ± 1	0.12
J021830.57-045622.9	0.081	10.46 ± 0.01	7.65 ± 0.04	0.7	5	29 ± 1	0.08
J021849.76-052158.2	1.560	13.07 ± 0.01	–	–	–	–	0.52
J021859.74-040237.2	0.008	8.18 ± 0.01	5.43 ± 0.02	3.5	3	27 ± 1	0.38
J021909.60-052512.9	0.068	10.96 ± 0.04	8.09 ± 0.03	1.5	5	29 ± 1	0.10
J021912.71-050541.8	0.025	9.23 ± 0.02	6.52 ± 0.07	2.5	3	–	0.30
J021916.05-055726.9	0.164	11.10 ± 0.02	7.91 ± 0.08	5.0	8	33 ± 1	0.00
J021928.33-042239.8	0.258	11.67 ± 0.03	8.50 ± 0.09	0.1	10	33 ± 2	0.18
J021938.70-032508.2	0.073	10.26 ± 0.02	7.33 ± 0.07	3.5	5	30 ± 1	0.00
J021939.08-051133.8	0.149	10.93 ± 0.01	7.55 ± 0.04	3.0	12	35 ± 1	0.16
J021953.04-051824.1	0.139	10.51 ± 0.01	7.83 ± 0.10	8.0	2	–	0.55
J021956.96-052440.4	0.239	11.25 ± 0.02	8.32 ± 0.04	4.0	5	31 ± 1	0.40
J022000.22-043947.6	0.708	12.67 ± 0.01	–	–	–	43 ± 1	0.40
J022005.93-031545.7	0.199	11.31 ± 0.02	8.33 ± 0.07	4.5	5	32 ± 1	0.01
J022012.21-034111.8	0.144	11.00 ± 0.01	7.87 ± 0.03	4.5	7	33 ± 1	0.04
J022145.09-053207.4	0.176	11.02 ± 0.01	7.43 ± 0.07	5.5	15	–	0.02
J022147.82-025730.7	0.143	11.08 ± 0.03	7.88 ± 0.07	1.0	10	–	0.19
J022147.87-044613.5	0.116	10.90 ± 0.02	7.77 ± 0.06	3.5	8	31 ± 1	0.14
J022151.54-032911.8	0.171	11.09 ± 0.01	7.58 ± 0.04	6.5	12	–	0.23
J022205.03-050537.0	2.068	13.35 ± 0.01	–	–	–	30 ± 2	0.54
J022223.26-044319.8	0.259	11.57 ± 0.02	8.29 ± 0.07	3.0	10	34 ± 7	0.18
J022224.06-050550.3	0.252	11.21 ± 0.02	–	–	–	32 ± 1	0.19
J022241.34-045652.0	0.096	10.89 ± 0.02	8.10 ± 0.05	0.0	5	29 ± 1	0.00
J022257.96-041840.8	0.063	10.69 ± 0.04	7.80 ± 0.03	2.0	5	29 ± 1	0.06
J022301.97-052335.8	0.105	10.61 ± 0.02	7.97 ± 0.06	6.0	2	28 ± 1	0.09
J022309.31-052316.1	0.144	11.27 ± 0.01	8.22 ± 0.07	2.5	7	31 ± 1	0.00
J022315.58-040606.0	0.053	11.02 ± 0.05	8.00 ± 0.05	0.4	8	31 ± 1	0.08
J022329.13-043209.5	0.150	11.15 ± 0.01	7.72 ± 0.07	0.5	15	36 ± 1	0.12
J022334.65-035229.4	0.044	10.62 ± 0.01	7.39 ± 0.02	6.5	8	32 ± 1	0.23
J022345.04-054234.4	0.205	11.28 ± 0.03	8.27 ± 0.06	2.0	7	32 ± 6	0.17
J022356.49-025431.1	0.056	10.13 ± 0.02	7.25 ± 0.10	2.0	5	29 ± 1	0.09
J022413.64-042227.8	0.055	10.59 ± 0.03	7.68 ± 0.05	2.5	5	29 ± 6	0.10
J022422.48-040230.5	0.057	10.72 ± 0.01	–	–	–	38 ± 1	0.68
J022431.58-052818.8	0.070	10.42 ± 0.03	7.26 ± 0.07	4.0	8	–	0.11
J022434.28-041531.2	0.135	10.66 ± 0.01	–	–	–	–	0.26
J022438.97-042706.3	0.055	11.02 ± 0.01	7.86 ± 0.03	4.0	8	32 ± 1	0.16
J022446.99-040851.3	0.173	11.07 ± 0.01	7.51 ± 0.03	2.0	20	–	0.21
J022457.64-041417.9	0.055	10.51 ± 0.02	7.79 ± 0.07	0.7	4	27 ± 1	0.10
J022507.43-041835.7	0.251	11.80 ± 0.01	8.82 ± 0.09	0.7	7	31 ± 1	0.00
J022508.33-053917.7	0.091	10.85 ± 0.01	7.86 ± 0.07	5.5	5	31 ± 1	0.14
J022522.59-045452.2	1.537	13.13 ± 0.01	–	–	–	46 ± 2	0.74
J022536.44-050011.5	0.885	12.57 ± 0.01	–	–	–	35 ± 1	0.42
J022548.21-050051.5	0.176	11.27 ± 0.01	8.27 ± 0.05	1.5	7	31 ± 1	0.01
J022549.78-040024.6	0.087	10.48 ± 0.01	7.12 ± 0.08	2.5	12	–	0.00
J022559.99-050145.3	0.100	10.54 ± 0.02	7.86 ± 0.07	2.5	3	28 ± 2	0.13
J022602.92-045306.8	0.140	10.94 ± 0.01	7.88 ± 0.05	3.0	7	32 ± 1	0.00
J022603.61-045903.8	1.285	13.20 ± 0.01	–	–	–	54 ± 1	0.78
J022617.43-050443.4	0.205	11.12 ± 0.01	7.83 ± 0.03	8.0	8	–	0.36
J022637.79-035841.6	0.178	10.74 ± 0.02	6.56 ± 3.71	90.0	10	–	0.24
J022655.87-040302.2	0.118	10.80 ± 0.01	7.73 ± 0.04	2.0	8	–	0.08
J022720.68-044537.1	0.072	9.91 ± 0.01	–	–	–	–	0.56
J022738.53-044702.7	0.925	12.32 ± 0.01	–	–	–	–	0.66

Notes. [a] Derived based on the DL07 model. [b] Derived based on MBB. [c] The uncertainties of the fractions as derived by the SED decomposition using DECOMPIR, are ≥10%.

Table 2. continued.

Name	$z_{\rm spec}$	$\log L_{\rm IR}$ $[L_\odot]$	$\log M_{\rm dust}$ [a] $[M_\odot]$	γ –	$U_{\rm min}$ –	$T_{\rm d}$ [b] [K]	AGN[c] frac.
J022741.64-045650.5	0.346	11.75 ± 0.01	7.94 ± 0.03	10.0	20	–	0.13
J103237.44+580845.9	0.360	11.91 ± 0.01	–	–	–	–	0.52
J103450.50+584418.2	1.468	12.81 ± 0.01	–	–	–	–	0.64
J103513.72+573444.6	0.067	10.94 ± 0.02	8.04 ± 0.06	2.0	5	30 ± 7	0.00
J103527.20+583711.9	0.025	10.44 ± 0.04	7.46 ± 0.04	1.0	7	30 ± 6	0.11
J103531.46+581234.2	0.118	11.00 ± 0.07	8.39 ± 0.10	0.9	3	26 ± 1	0.14
J103542.76+583313.1	0.322	11.44 ± 0.01	–	–	–	–	0.42
J103601.81+581836.2	0.140	10.90 ± 0.02	8.37 ± 0.07	3.0	2	27 ± 1	0.15
J103606.45+581829.7	0.391	11.58 ± 0.01	–	–	–	–	0.95
J103646.42+584330.6	0.230	11.54 ± 0.02	8.75 ± 0.06	0.4	5	29 ± 1	0.11
J103701.99+574414.8	0.232	11.66 ± 0.02	8.66 ± 0.08	1.5	7	–	0.10
J103724.74+580512.9	0.162	11.02 ± 0.01	7.68 ± 0.05	5.0	10	–	0.00
J103803.35+572701.5	0.072	10.62 ± 0.01	7.60 ± 0.07	0.9	8	–	0.07
J103813.90+580047.3	0.119	11.13 ± 0.03	7.77 ± 0.06	5.0	10	34 ± 1	0.09
J103818.19+583556.5	0.131	10.86 ± 0.04	8.12 ± 0.05	0.9	4	29 ± 1	0.00
J103856.16+570333.9	0.768	12.23 ± 0.01	–	–	–	–	0.39
J104016.32+570846.0	0.073	10.40 ± 0.01	7.06 ± 0.06	4.5	10	34 ± 1	0.00
J104058.79+581703.3	1.814	13.16 ± 0.01	–	–	–	–	0.51
J104131.79+592258.4	0.115	10.78 ± 0.01	7.28 ± 0.08	6.5	12	36 ± 1	0.13
J104132.49+565953.0	0.117	11.31 ± 0.01	8.49 ± 0.06	0.7	5	29 ± 1	0.12
J104159.83+585856.4	0.460	11.92 ± 0.01	8.99 ± 0.21	20.0	2	–	0.08
J104255.66+575549.7	1.101	12.50 ± 0.02	–	–	–	–	0.83
J104303.50+585718.1	0.205	11.47 ± 0.01	–	–	–	32 ± 1	0.37
J104432.94+564041.6	1.211	12.98 ± 0.02	–	–	–	49 ± 1	0.78
J104438.21+562210.7	0.047	10.22 ± 0.01	7.25 ± 0.09	0.4	7	31 ± 1	0.00
J104454.08+574425.7	0.130	11.00 ± 0.02	7.98 ± 0.09	2.0	7	30 ± 6	0.00
J104501.73+571111.3	0.140	11.19 ± 0.02	–	–	–	30 ± 1	0.58
J104516.02+592304.7	0.086	10.32 ± 0.01	6.83 ± 0.07	2.5	15	–	0.08
J104643.26+584715.1	0.073	10.26 ± 0.01	7.31 ± 0.07	4.0	5	–	0.00
J104705.07+590728.4	0.119	10.87 ± 0.02	7.54 ± 0.09	10.0	8	33 ± 1	0.31
J104729.89+572842.9	2.335	13.40 ± 0.02	–	–	–	30 ± 1	0.62
J104837.81+582642.1	0.453	11.78 ± 0.01	–	–	–	–	0.38
J104839.73+555356.4	0.387	12.02 ± 0.01	8.26 ± 0.02	8.0	20	–	0.07
J104843.90+580341.2	0.243	11.26 ± 0.01	8.22 ± 0.06	6.5	5	33 ± 1	0.08
J104907.15+565715.3	0.277	11.81 ± 0.01	8.75 ± 0.04	1.5	8	33 ± 2	0.00
J104918.33+562512.9	0.226	11.25 ± 0.01	–	–	–	29 ± 1	0.36
J105005.97+561500.0	0.226	11.46 ± 0.01	7.83 ± 0.02	3.5	20	–	0.08
J105047.83+590348.3	0.260	11.52 ± 0.02	8.29 ± 0.04	1.5	10	34 ± 2	0.07
J105058.76+560550.0	0.214	11.26 ± 0.02	–	–	–	34 ± 1	0.20
J105106.12+591625.3	0.053	10.35 ± 0.04	7.78 ± 0.05	0.0	3	26 ± 1	0.00
J105128.05+573502.4	0.065	10.27 ± 0.02	7.58 ± 0.03	3.0	3	28 ± 3	0.01
J105158.53+590652.0	0.066	10.34 ± 0.01	7.52 ± 0.02	2.5	4	29 ± 1	0.00
J105200.29+591933.7	0.065	10.56 ± 0.03	7.76 ± 0.03	0.2	5	29 ± 2	0.00
J105206.56+580947.1	0.084	10.62 ± 0.01	7.80 ± 0.03	1.0	5	28 ± 1	0.00
J105336.87+580350.7	0.068	10.30 ± 0.02	7.53 ± 0.04	1.5	4	29 ± 1	0.00
J105404.11+574019.7	0.082	10.61 ± 0.04	7.81 ± 0.05	0.2	5	–	0.00
J105421.65+582344.6	0.086	10.68 ± 0.03	7.96 ± 0.04	0.6	4	28 ± 1	0.00
J105604.84+574229.9	0.063	10.20 ± 0.02	7.56 ± 0.03	1.5	3	–	0.16
J105636.95+573449.3	0.078	10.40 ± 0.02	7.36 ± 0.05	1.0	8	31 ± 1	0.00
J105641.81+580046.0	0.138	11.05 ± 0.01	7.78 ± 0.03	10.0	7	34 ± 3	0.24
J105705.43+580437.4	0.083	10.72 ± 0.03	8.22 ± 0.02	2.0	2	26 ± 1	0.00
J105733.53+565737.4	0.035	9.54 ± 0.01	6.44 ± 0.04	2.5	8	31 ± 1	0.00
J105740.55+570616.4	0.048	10.40 ± 0.02	7.20 ± 0.02	0.9	10	33 ± 1	0.00
J105829.28+580439.2	0.065	10.59 ± 0.03	8.17 ± 0.06	0.6	2	–	0.00
J105854.08+574130.0	0.180	10.86 ± 0.01	–	–	–	27 ± 1	0.17
J105903.47+572155.1	0.305	11.73 ± 0.03	8.30 ± 0.06	4.0	12	36 ± 1	0.22
J105951.71+581802.9	0.474	11.59 ± 0.01	–	–	–	–	0.43
J105959.95+574848.1	0.215	11.49 ± 0.01	8.36 ± 0.03	3.0	8	–	0.00
J110002.06+573142.1	0.223	11.28 ± 0.01	–	–	–	–	0.51
J110124.97+574315.8	0.135	11.15 ± 0.01	–	–	–	38 ± 2	0.67
J110133.80+575206.6	0.083	11.16 ± 0.04	8.31 ± 0.03	0.9	5	29 ± 1	0.00
J110223.58+574436.2	0.281	11.42 ± 0.01	8.22 ± 0.02	6.5	8	–	0.21
J110235.02+574655.7	0.210	11.63 ± 0.01	8.55 ± 0.03	1.5	8	32 ± 2	0.00
J160408.18+542531.2	1.663	12.88 ± 0.01	–	–	–	–	0.76
J160630.59+542007.4	0.217	11.26 ± 0.01	7.68 ± 0.05	2.5	20	–	0.23

Table 2. continued.

Name	$z_{\rm spec}$	$\log L_{\rm IR}$ $[L_\odot]$	$\log M_{\rm dust}$ [a] $[M_\odot]$	γ –	$U_{\rm min}$ –	$T_{\rm d}$ [b] [K]	AGN[c] frac.
J160655.35+534016.9	0.079	10.59 ± 0.01	7.98 ± 0.00	1.0	3	27 ± 1	0.00
J160803.71+545301.9	0.167	11.19 ± 0.01	7.56 ± 0.00	4.0	20	–	0.25
J160832.59+552926.9	2.990	13.14 ± 0.02	–	–	–	–	0.00
J160839.73+552330.6	0.129	11.11 ± 0.01	8.05 ± 0.07	2.0	8	32 ± 1	0.00
J160858.38+553010.2	0.257	11.57 ± 0.01	8.18 ± 0.01	3.0	12	–	0.34
J160907.56+552428.4	0.248	11.28 ± 0.01	8.45 ± 0.07	3.5	4	31 ± 9	0.04
J160908.28+552241.4	0.066	10.25 ± 0.02	–	–	–	24 ± 1	0.83
J160926.69+551642.3	0.153	11.25 ± 0.02	8.25 ± 0.07	1.5	7	31 ± 1	0.00
J160931.55+541827.3	0.107	10.62 ± 0.05	7.45 ± 0.09	5.0	8	–	0.22
J160937.48+541259.2	0.182	10.81 ± 0.01	8.04 ± 0.09	60.0	0	–	0.20
J161103.73+544322.0	0.110	10.82 ± 0.01	7.74 ± 0.07	3.5	7	31 ± 1	0.00
J161123.44+545158.2	0.248	10.84 ± 0.01	–	–	–	–	0.56
J161223.39+540339.2	0.322	11.90 ± 0.01	–	–	–	–	0.58
J161233.43+545630.4	0.139	11.22 ± 0.02	8.03 ± 0.09	0.4	10	33 ± 1	0.22
J161241.05+543956.8	0.069	10.73 ± 0.01	7.52 ± 0.10	1.0	10	–	0.00
J161250.85+532304.9	0.125	11.11 ± 0.02	8.13 ± 0.11	1.0	7	30 ± 1	0.00
J161254.17+545525.4	1.697	12.91 ± 0.01	–	–	–	–	0.56
J161357.01+534105.3	0.028	9.76 ± 0.01	7.07 ± 0.07	0.4	4	27 ± 1	0.00
J161411.52+540554.3	0.272	11.22 ± 0.01	–	–	–	–	0.30
J161521.78+543148.3	0.742	12.34 ± 0.01	–	–	–	–	0.55
J161551.45+541535.9	1.624	13.08 ± 0.01	–	–	–	–	0.43
J161645.92+542554.4	0.108	10.74 ± 0.02	7.52 ± 0.19	1.5	10	32 ± 1	0.20
J161759.22+541501.3	0.175	11.15 ± 0.01	8.28 ± 0.05	2.0	5	30 ± 1	0.11
J161819.31+541859.0	0.030	9.33 ± 0.01	6.24 ± 0.03	4.0	7	–	0.29
J171033.21+584456.8	0.156	11.10 ± 0.01	7.97 ± 0.01	3.5	8	–	0.00
J171124.22+593121.4	0.035	10.47 ± 0.02	7.79 ± 0.08	0.0	4	27 ± 1	0.05
J171232.34+592125.9	0.029	10.25 ± 0.01	7.22 ± 0.04	0.7	8	30 ± 1	0.05